Geological Magazine

www.cambridge.org/geo

Original Article

Cite this article: Zhao C, Sun J, Liu Y, Chu X, Xu Z, Han J, Li W, Ren L, and Bai C (2021) Constraints of magmatism on the Ergu Fe–Zn polymetallic metallogenic system in the central Lesser Xing'an Range, NE China: evidence from geochronology, geochemistry and Sr–Nd–Pb–Hf isotopes. *Geological Magazine* **158**: 1862–1890. https://doi.org/10.1017/S0016756821000479

Received: 29 December 2020
Revised: 22 April 2021
Accepted: 12 May 2021
First published online: 23 July 2021

Keywords:
element geochemistry; Sr–Nd–Pb–Hf isotope geochemistry; zircon U–Pb dating; intermediate-plutonic magmatism; Ergu deposit; Lesser Xing'an Range

Author for correspondence:
Jinggui Sun, Email: sunjinggui@jlu.edu.cn

CAMBRIDGE UNIVERSITY PRESS

Constraints of magmatism on the Ergu Fe–Zn polymetallic metallogenic system in the central Lesser Xing'an Range, NE China: evidence from geochronology, geochemistry and Sr–Nd–Pb–Hf isotopes

Chuntao Zhao[1,2], Jinggui Sun[1,2], Yang Liu[1], Xiaolei Chu[1], Zhikai Xu[1], Jilong Han[3], Wenqing Li[2], Liang Ren[1] and Chenglin Bai[1]

[1]College of Earth Science, Jilin University, Changchun 130061, China; [2]Key Laboratory of Mineral Resources Evaluation in Northeast Asia, Ministry of Natural Resources, Changchun 130061, China and [3]School of Earth Sciences and Resources, China University of Geosciences, Beijing 100083, China

Abstract

The medium-sized Ergu Fe–Zn polymetallic skarn deposit is located in the central Lesser Xing'an Range, NE China. The ore bodies are mainly hosted in the contact zone between granodiorite intrusions and lower Cambrian dolomitic crystalline limestones or skarns. To reveal the magmatic influence on the mineralization, resource potential and metallogenic geodynamic process of this deposit, a systematic study of the geology, petrology, zircon U–Pb dating, element geochemistry, amphibole geochemistry and Sr–Nd–Pb–Hf isotopes of the Ergu deposit intrusives was conducted. The results show the following: (1) The major rock types in the mine area are medium-grained granodiorite and porphyritic granite, and the rock related to mineralization is medium-grained granodiorite. Zircon U–Pb dating suggests that the granodiorite and porphyritic granite formed at 181.9–183.8 Ma and 182.7 Ma, respectively. Thus, an Early Jurassic magmatic event led to the formation of the Ergu deposit. (2) The granodiorite and porphyritic granite are high-K calc-alkaline I-type granites that formed by comagmatic evolution with varying degrees of fractional crystallization and were likely derived from partial melting of the lower crust. The Ergu deposit occurred in an active continental-margin tectonic setting. (3) The high water content (5.69 wt % H_2O), high oxygen fugacity ($\Delta FMQ = +1.75$ to $+1.82$) and intermediate-plutonic emplacement (3.13 km) of the granodioritic magma are key factors in the formation of the Ergu deposit. The porphyry granite is characterized by high water content (>4 wt % H_2O), reduced oxygen fugacity ($\Delta FMQ = -0.47$) and shallow emplacement (<3 km).

1. Introduction

Skarn is widely known to host important W, Cu, Fe, Zn, Pb, Ag, Au and Sn deposits (Hedenquist & Lowenstern, 1994; Meinert *et al.* 2005). Numerous economic geologists have studied the mineralization, metallogenic specialization and metallogenic models of skarn deposits (Newberry and Swanson, 1986; Xie *et al.* 2015). Recent studies indicate that the development and fertility of a particular skarn deposit depend on various parameters, such as the acidity and alkalinity of the magma (Meinert *et al.* 2005; Ren *et al.* 2017), the degree of crystallization differentiation (Meinert *et al.* 2005; Fei *et al.* 2018), the emplacement depth of the magma (Zhang *et al.* 2007), the volatile content (Zhong *et al.* 2018) and the oxygen fugacity (Chappell & White, 2001). Therefore, to evaluate the resource potential of a particular deposit, analyses of the magmatic properties of the metallogenic system and the constraints of magmatism on mineralization have become major topics in this field (Sun *et al.* 2013).

The Lesser Xing'an Range is located in the eastern part of the Central Asian Orogenic Belt (CAOB) and is one of the areas with skarn deposits in China. In recent years, we have observed that in the Lesser Xing'an Range, with the exception of the large Cuihongshan Fe-polymetallic deposit (Fe: 68.35 Mt, 48 %); Hu *et al.* 2014*a*), most skarn deposits have small reserves, such as the Baoshan Cu-polymetallic deposit (Cu: small-sized; Ren *et al.* 2017), Daxilin Fe deposit (Fe: small-sized; Li *et al.* 2015), Da'anhe Au deposit (Au: medium-sized; Yang, 2013), Xulaojiugou Pb–Zn deposit (Pb: 54 707 t, 2.18 %; Zn: 107 259 t, 2.06 %; Hu *et al.* 2014*b*) and Ergu Fe–Zn polymetallic deposit (Fe: 17.31 Mt, 35 %; Ren *et al.* 2017). Numerous scientific studies have focused on the chronology and metallogenic dynamics of these deposits to establish the metallogenic dynamics framework of the area and to determine the timing and spatial scope of the Palaeo-Asian and Circum-Pacific tectonic systems (Tan, 2013; Xu *et al.* 2013). However,

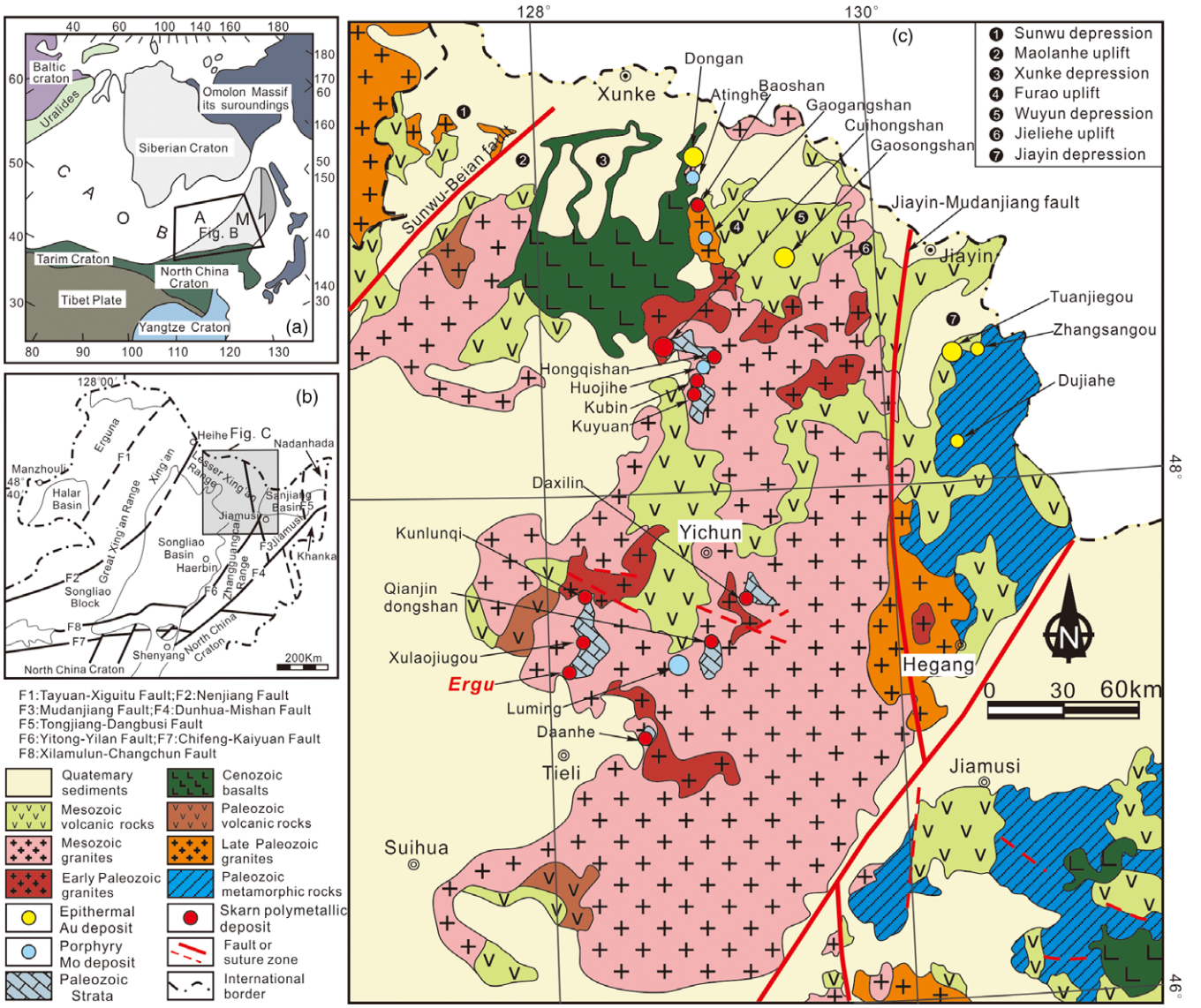

Fig. 1. (Colour online) (a) Location of NE China with respect to the main tectonic units of China and Russia, modified after Wu *et al.* (2007). 'A' and 'M' represent the Altaids and Manchrids. (b) Tectonic sketch maps of NE China, modified after Wu *et al.* (2000). (c) Simplified geological map of the Lesser Xing'an range, modified after Wu *et al.* (2011).

the core problem concerning which magmatic properties can restrict mineralization and resource potential is seldom discussed.

The Ergu Fe–Zn polymetallic deposit, located in the central Lesser Xing'an Range, is a representative skarn deposit and a good candidate for determining the constraints that magmatism imposes on skarn polymetallic deposits. In this study, we report new data on the geochronology, geochemistry and Sr–Nd–Pb–Hf isotopic compositions of intrusives in mining areas. Based on these data, in combination with previous work, we conclude that the magmatism and mineralization of the Ergu deposit occurred during the Early Jurassic and were likely related to the magmatic arc system of the continental margin in eastern China where the Palaeo-Pacific Plate was subducting beneath Eurasia in the Mesozoic. In addition, we determined that the high water content, high oxygen fugacity and medium-deep emplacement of the granodioritic magma were the key factors in the formation of the medium-sized Fe–Zn polymetallic skarn deposit in this area.

2. Regional geology

The central Lesser Xing'an Range is located in the eastern segment of the CAOB, sandwiched between the Siberian Craton, North China Craton and Pacific Plate (Fig. 1a). The area has a complex tectonic history, including the evolution of the Palaeo-Asian Ocean, the effects of the Mesozoic subduction of the Palaeo-Pacific Plate, and Cenozoic supracrustal faulting (Jahn *et al.* 2000; Windley *et al.* 2007; Sun *et al.* 2012), resulting in a large number of magmatic, structural and mineralization events in this region (Fig. 1b, c).

The stratigraphy (Fig. 1c) of this region is dominated by the gold-bearing silicoferrite of the Dongfengshan Formation (821–801 Ma; Gao *et al.* 2013) and the overlying Cambrian–Ordovician neritic facies clastic rocks (limestone, dolomite marble, carbonaceous slate, etc.; ~500 Ma; Li, 1999), Permian terrigenous clastic-carbonate formations (amphibolite, marble, tuff, felsic schist and slate, etc.; Ren, 2017), Mesozoic continental volcanic rocks (including two stages: 190–170 Ma and 130–105 Ma), and

https://doi.org/10.1017/S0016756821000479 Published online by Cambridge University Press

Palaeogene fluvial and lacustrine clastic sedimentary rocks (Heilongjiang Bureau of Geology and Mineral Resources, 1993). Among them, the Palaeozoic strata are closely related to the mineralization of skarn-type deposits in the study area. The Lesser Xing'an Range is also characterized by voluminous Phanerozoic granitoids, which are distributed along a N–S-trending granite belt and are characterized by four periods: (1) Early Caledonian intrusions (490–417 Ma), (2) Late Hercynian granitoids (272–251 Ma), (3) Late Hercynian and Indosinian – Early Yanshanian plutonic rocks (225–175 Ma) (Wei, 2012; Yu *et al.* 2012; Wang *et al.* 2016) and (4) Late Yanshanian granitoids (154–101 Ma; Zhang, 2013; Han *et al.* 2019). Of these, the Late Hercynian and Indosinian – Early Yanshanian plutonic rocks are the most common and are closely related to skarn polymetallic deposits (Sun *et al.*, 2004; Wu *et al.* 2011; Hu *et al.* 2014*a*, *b*). The dominant regional structures are oriented to the NE and nearly N–S and include the Yitong–Yilan Fault, Dunhua–Mishan Fault and Jiayin–Mudanjiang Fault. These structures jointly control the distribution of igneous rocks and deposits, such as porphyry Mo deposits (e.g. Luming (Chen & Zhang, 2018); Huojihe (Hu *et al.* 2019); Cuiling and Gaosongshan (Hao *et al.* 2015)), epithermal gold deposits (Dong'an (Zhang *et al.* 2010); Gaosongshan (Liu *et al.* 2019); Yongxin (Zhao *et al.* 2019)) and skarn deposits (Cuihongshan (Zhang *et al.* 2018); Ergu and Baoshan (Ren, 2017)). Among them, the porphyry Mo deposits occur in the porphyry or in the late lithofacies of the granitic complex, with formation ages concentrated in the Early Jurassic (176–186 Ma). The epithermal deposits are mostly developed in the Early Cretaceous volcanic, subvolcanic or hypabyssal porphyry areas, with the mineralization mainly occurring from 110 to 95 Ma. Skarn deposits are mainly developed in the contact zone between the Palaeozoic strata and Mesozoic granite. Except for the Baoshan deposit, which formed in the Early Triassic (250.3 Ma), most skarn deposits formed in the Early–Middle Jurassic (179.9–203 Ma) (Fig. 1c).

3. Ore deposit geology

The Ergu Fe–Zn polymetallic deposit is located in the central Lesser Xing'an Range, NE China. The deposit was discovered by aeromagnetic anomalies in the ground in 1960 and yielded proven resources of 15.8 Mt Fe, 0.021 Mt Cu, 0.03 Mt Mo, 0.23 Mt Zn and 0.13 Mt Pb, with average grades of 34.66 % Fe, 0.54 % Cu, 0.05 % Mo, 3.9 % Zn and 3.4 % Pb. Additionally, the skarn deposits contain other economic components, such as In, Ga and Ag (Ren, 2017).

The exposed strata in the mining area are typically the lower Cambrian Qianshan and Laodaogoumiao Formations, which consist of crystalline limestone and marble, silty slate and hornstone, respectively. In addition, the Permian Wudaoling Formation and Quaternary are also well developed in the mining area, consisting of dacitic tuffaceous lava and alluvial sediments, respectively (Fig. 2a). The unit closely related to mineralization is the Qianshan Formation. Because the early Palaeozoic strata in the mining area were destroyed by the influence of magmatic and structural activity, they are mostly in the form of captured bodies with scattered and irregular distributions. The intrusions in the mining area are widely distributed, occupying *c.* 80 % of the mining area. The main lithologies are Early Jurassic medium-grained granodiorite and porphyry granite, which are different lithofacies evolved from the magma of the same period, and all occur in the shape of rock stock (Ren, 2017). In addition, there are a few late diorite dikes. The main ore-controlling structure in the mining area is the Xulaojiugou–Ergu anticline oriented in the N–S direction. The ore bodies mainly occur at the contact between the Qianshan Formation and the granodiorite, and there are three ore zones, including Xishan, Xiangshuihe and Dongshan (Fig. 2a).

To date, a total of 21 cystiform, lenticular or veined ore bodies have been discovered, with a length of 30–887 m, a width of 0.92–13.9 m and a maximum extension depth of 556 m. These ore bodies occur in the inner, middle and outer zones of the contact zone between the granodiorite and carbonate rocks of the lower Cambrian Qianshan Formation (Fig. 2). The developed ore bodies are magnetite ore bodies; magnetite–sphalerite ore bodies formed by quartz veinlets containing sphalerite-penetrating magnetite; pyrrhotite–pyrite–arsenopyrite ore bodies; copper polymetallic ore bodies; and galena–sphalerite ore bodies. Of these, the magnetite ore bodies and magnetite–sphalerite ore bodies are relatively developed. Therefore, the Ergu deposit is a skarn Fe–Zn polymetallic deposit. The attitudes of the deposits are obviously controlled by associated structures, and the ore bodies feature a wavy distribution in cross section. Generally, when the contact zone between the granodiorite and the carbonate of the Qianshan Formation exhibits a shallower dip or curves, the thickness of the ore body clearly increases. These ore bodies developed in the contact zone near the granodiorite intrusion (1–28 m) are mainly enriched in Fe and Cu, and those far from the granodiorite intrusion (15–87 m) are mainly enriched in Pb and Zn (Fig. 2b, c).

The medium-grained granodiorite related to mineralization has an exposed area of ~10 km^2 and occurs in the form of batholith or stock (Fig. 2a). The medium-grained granodiorite is white-grey in colour, with a medium-grained granitic texture ($d = 2$–5 mm) and a massive structure. The rock is composed of plagioclase (35–40 %), K-feldspar (20–25 %), quartz (20–25 %), amphibole (5–10 %) and biotite (~5 %), with accessory magnetite, zircon and apatite (Fig. 3a, b). The amphibole crystals (0.5–1.5 mm) are mainly light green to dark green, occur as isolated crystals and show uniform and weak opacification (Fig. 3c, d), which records the physicochemical information of deep crystallizing magmas (Chambefort *et al.* 2013). The porphyritic granite is off-white to light pink in colour and has a fine-grained porphyritic texture defined by 35–40 % phenocrysts. Phenocrysts are composed of K-feldspar (35–40 %), quartz (25–30 %), plagioclase (20–25 %) and biotite (~5 %). The groundmass is dominated by quartz, K-feldspar plagioclase and biotite. The porphyritic granite also contains accessory zircon and apatite (Fig. 3b, d). The main wall-rock alterations are silicification, skarnization, epidotization, carbonation and fluoritization, and there is a small amount of chloritization, potassium and sericitization. Generally, the closer to the skarn belt, the stronger the wall-rock alteration. The gangue minerals consist of garnet (Fig. 4a, d), diopside (Fig. 4c, d), epidote (Fig. 4b, c, g), quartz and calcite (Fig. 4d, e), with minor chlorite, fluorite, phlogopite and actinolite. The ore structures are typically massive and disseminated, with some also exhibiting stockwork and banding. The ore minerals are dominated by magnetite (Fig. 4b, e), chalcopyrite (Fig. 4g, h), pyrite (Fig. 4g, h), molybdenite (Fig. 4f), pyrrhotite (Fig. 4g, h) and sphalerite (Fig. 4i), with minor galena (Fig. 4i), scheelite and malachite.

4. Samples and analytical methods

On the basis of detailed field geological work and petrographic observations, two medium-grained granodiorite samples

https://doi.org/10.1017/S0016756821000479 Published online by Cambridge University Press

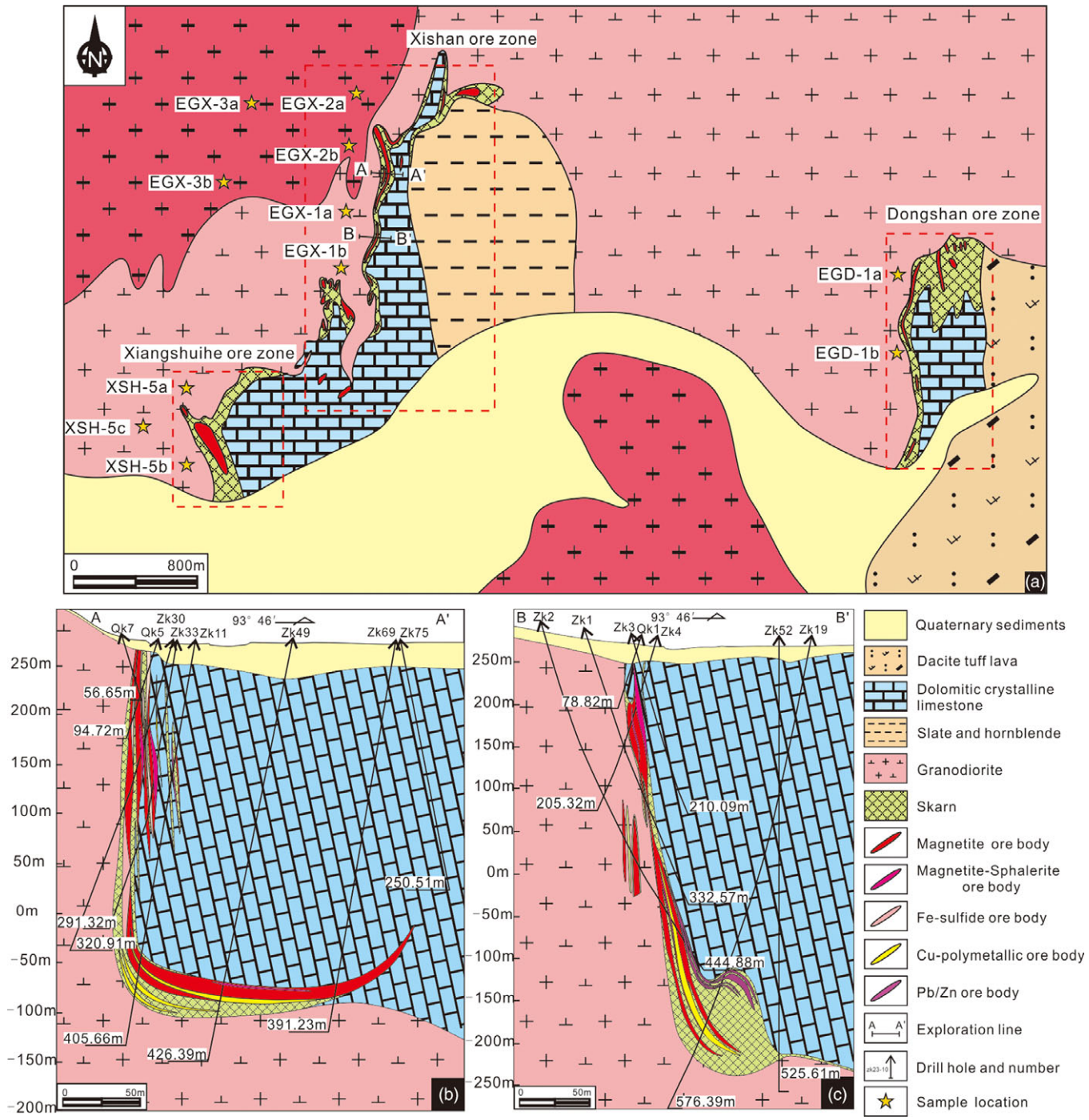

Fig. 2. (Colour online) (a) Simplified geological map of the Ergu Fe–Zn polymetallic deposit; (b, c))cross section of the Ergu Fe–Zn polymetallic deposit (sketch modified after Ren, 2017).

(EGX-1 and XSH-5) and two porphyritic granite samples (EGX-2 and EGX-3) were chosen for zircon U–Pb dating, and samples EGX-1, XSH-5 and EGX-2 were chosen for *in situ* Hf isotopic analysis. Seven medium-grained granodiorite samples and four porphyritic granite samples were collected for major and trace element analyses. Seven medium-grained granodiorite samples (EGX-1 and XSH-5) were collected for electron microprobe analysis of amphibole. A total of four medium-grained granodiorite samples were chosen for Sr–Nd–Pb isotopic analysis (sampling locations are marked in Fig. 2).

4.a. Zircon U–Pb dating and Lu–Hf isotope analyses

Zircons were extracted from representative medium-grained granodiorite samples (EGX-1 and XSH-5) and porphyritic granite samples (EGX-2 and EGX-3) using standard density and magnetic separation techniques followed by handpicking using a binocular microscope at the Langfang Regional Geological Survey, Hebei Province, China. Many zircons were handpicked from the samples pasted on the resin disc under the binocular microscope, and then polished to expose the grain centres. Cathodoluminescence (CL) images of the zircon grains were taken using a Mono CL3 detector

https://doi.org/10.1017/S0016756821000479 Published online by Cambridge University Press

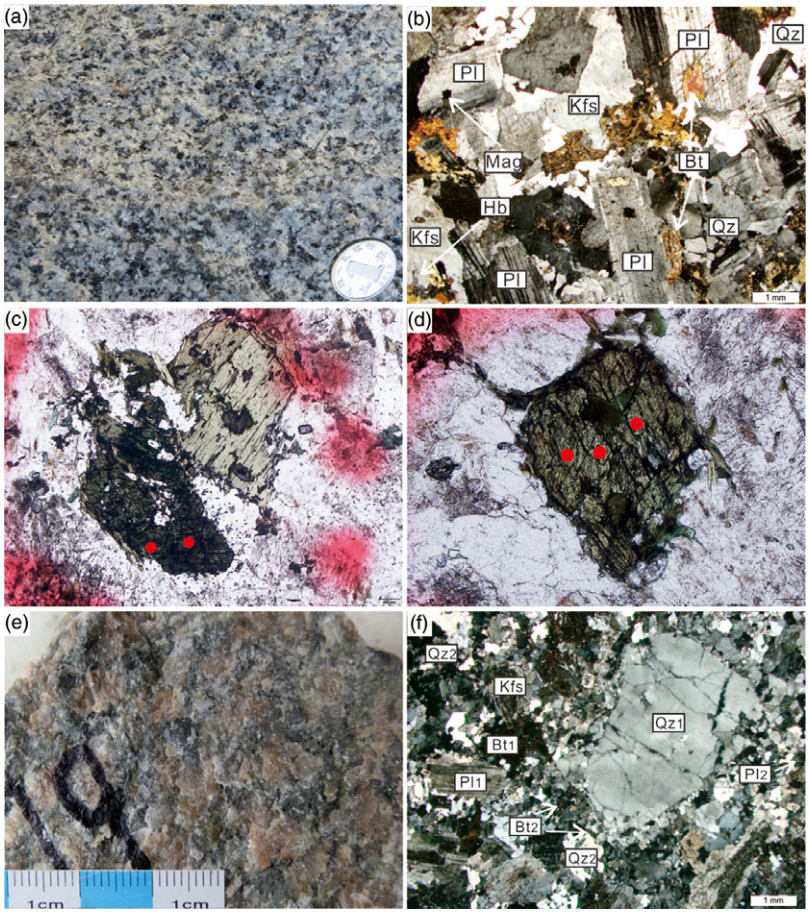

Fig. 3. (Colour online) (a) Hand specimen photograph and (b) photomicrographs of granodiorite with massive structures; (c, d) Light green, euhedral amphibole crystals in the granodiorite. (e) Hand specimen photograph and (f) photomicrographs of porphyritic granite with massive structures. Bt = biotite; Kfs = K-feldspar; Pl = plagioclase; Q = quartz; Hb = amphibole; Mag = magnetite.

(manufactured by Gatan USA) attached to a scanning electron microscope (manufactured by JSM6510, JEOL, Japan) at the Nanjing Hongchuang. Exploration Technology Service Co., Ltd. After CL images were taken with a JEOL scanning electron microscope, the zircon grains were subjected to *in situ* U–Pb dating and Hf isotope analysis.

Analysis of zircon trace elements was carried out using an Agilent 7900 inductively coupled plasma mass spectrometer (ICP-MS) instrument coupled with a 193 nm ArF excimer laser (COMPexPro 102, Coherent, DE) with the automatic positioning system at the MLR Key Laboratory of Mineral Resources Evaluation in Northeast Asia, Jilin University, Changchun, China. During analysis, the laser spot size was set to 32 μm for most analyses, the laser energy density was set to 10 J cm^{-2} and the repetition rate was set to 8 Hz, with data acquired over a duration of 80–120 s. Calibrations for elemental concentration analysis in zircon were performed using NIST 610 glass as an external standard and ^{29}Si as an internal standard. U–Pb isotope fractionation effects were corrected using the zircon standard Plesovice (337 Ma) as an external standard. The zircon standard 91500 was used as a secondary standard to monitor the deviation in age measurement/calculation. The trace element compositions of zircons were calibrated against NIS610 combined with the internal standardization of Si. Isotopic ratios and element concentrations of zircons were calculated using GLITTER (ver. 4.4.2, Macquarie University). Concordia diagrams were constructed using Isoplot/Ex (3.0) (Ludwig, 2003). Common lead was corrected using (laser ablation) LA-ICP-MS Common Lead Correction (ver. 3.15), following the method of Andersen (2002). The analytical data are presented on U–Pb concordia diagrams with 2σ errors. The mean ages are weighted means at 95 % confidence levels.

In situ zircon Hf isotopic analyses were conducted on the same spots or on the same zircon zones where U–Pb age determinations were made. *In situ* Hf isotope ratio analysis experiments were conducted using a Thermo Finnigan Neptune (multicollector) MC-ICP-MS system coupled to a New Wave UP 193 nm laser ablation system at the Laboratory of Isotope Geology, Tianjin Institute of Geology and Mineral Resources, Tianjin, China. A laser repetition rate of 11 Hz at 100 mJ was used for ablating zircons, and the laser beam diameter was 50 um. Helium was used as the carrier gas for the ablated aerosol. Details of the instrumental conditions and analytical procedures for Lu–Hf isotope analyses are described by Geng *et al.* (2017). Isotopes, including ^{177}Hf, ^{178}Hf, ^{179}Hf, ^{180}Hf, ^{172}Yb, ^{173}Yb, ^{175}Lu, $^{176}(Hf + Yb + Lu)$, and ^{182}W, were measured during the analytical process. All Lu–Hf isotope results are reported with 2σ uncertainties. In this study, the detailed operating conditions for the laser ablation system and the MC-ICP-MS instrument and analytical method were the same as those described by Geng *et al.* (2017).

4.b. Electron microprobe analysis of amphibole

The rock-forming minerals (three amphiboles) from two granodiorite samples (EGX-1 and XSH-5) were analysed for their chemical composition using a JEOL JEOL-8100 electron microprobe (EPMA) at the Electron Probe Laboratory of Northeast Asia, Ministry of Land and Resources of China, Changchun, China. Measurements were performed using a voltage of 20 kV and a

https://doi.org/10.1017/S0016756821000479 Published online by Cambridge University Press

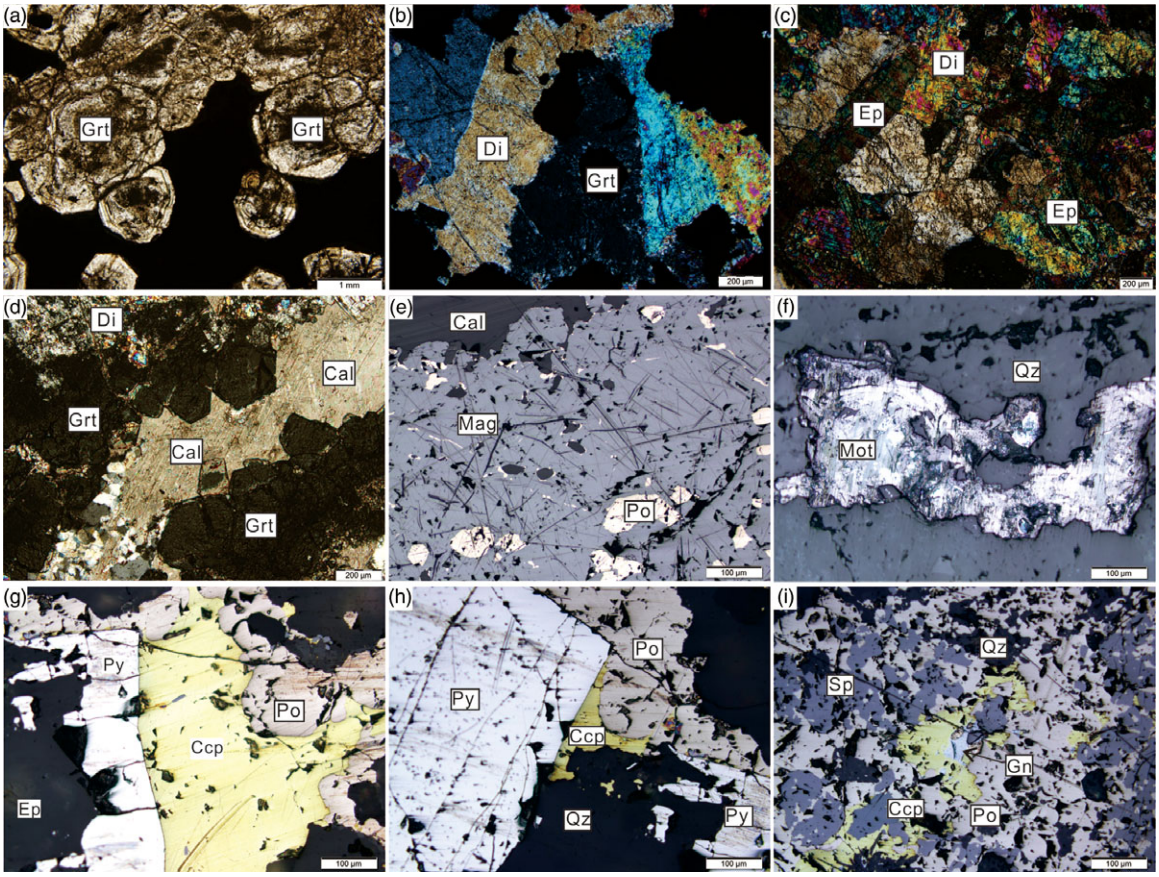

Fig. 4. (Colour online) Photomicrographs of skarn and mineralization features in the Ergu Fe–Zn polymetallic deposit. (a) A typical zoned garnet crystal; (b) epidote and magneitite intergrowth; (c) tufted epidote crystal; (d) early garnet and diopside minerals are cut by calcite veins;(e) microscopic picture of magnetite replaced by pyrrhotite; (f) irregular molybdenite crystal; (g) microscopic picture of paragenetic pyrite and chalcopyrite; (h) mineral assemblage consisting of pyrite, chalcopyrite and pyrrhotite; (i) mineral assemblage consisting of pyrite, galena, sphalerite and chalcopyrite. Grt = garnet; Di = diopside; Ep = epidote; Cal = calcite; Mag = magnetite; Ccp = chalcopyrite; Py = pyrite; Mot = molybdenite; Po = pyrrhotite; Sp = sphalerite; Gn = galena.

current of 1×10^{-8} A. The measuring time was 10 s and the results were corrected using the ZAF algorithm. The following mineral standards, recommended by the American National Standard Mineral Bureau, were used for quality control: rutile for Ti; diopside for Si, Mg and Ca; orthoclase for K; albite for Na and Al; almandine for Fe; and crocoite for Cr.

4.c. Major and trace element determinations

The whole-rock sample analysis experiment was completed in the Geological Laboratory of Hebei Regional Institute of Geology and Mineral Resources. Prior to geochemical and isotopic analysis, the rock samples were washed with pure water, dried and crushed into powder of less than 200 mesh. Major and trace elements were obtained at the Beijing Research Institute of Uranium Geology, Beijing, China. Major element analyses were determined by X-ray fluorescence using a Rigaku RIX 2100 spectrometer with analytical uncertainties of 1–5 %. Trace element compositions were determined using a PEE lan 6000 ICP-MS with analytical uncertainties of 1–3 %. Details of the analytical technique are described by Rudnick *et al.* (2004) and Li *et al.* (2005).

4.d. Sr–Nd–Pb isotopic analyses

The Rb–Sr, Sm–Nd and Pb isotopic compositions were determined by isotope dilution methods. The measurements were performed on a Finnigan MAT thermal ionization mass spectrometer (Triton TI) at the State Key Laboratory for Mineral Deposits Research, Nanjing University, China. Dissolution and chemical separation of Sm–Nd and Rb–Sr samples were performed using a procedure similar to that described in Pu *et al.* (2005). All Sr data are corrected for mass fractionation to $^{86}Sr/^{87}Sr = 0.1194$ and reported relative to a value of $^{87}Sr/^{86}Sr = 0.705018 \pm 0.000003$ (2σ) for the BCR-2 standard. In the Nd isotopic analysis, $^{146}Nd/^{144}Nd = 0.7219$ was taken as the standard for mass fractionation correction, and Nd isotopic ratios were normalized to a value of $^{143}Nd/^{144}Nd = 0.511842 \pm 0.000004$ (2σ) for La Jolla. The $\epsilon Nd(t)$ values and $f_{Sm/Nd}$ and Nd model ages were calculated assuming $^{147}Sm/^{144}Nd$ and $^{143}Nd/^{144}Nd$ ratios for average chondrite and the depleted mantle at the present day to be 0.1967 and 0.512638 and 0.2137 and 0.51315, respectively (Hamilton *et al.* 1983). λ_{Rb} and λ_{Sm} are 1.42×10^{-11} year^{-1} and 6.54×10^{-12} year^{-1}, respectively (Lugmair & Harti, 1978).

Whole-rock Pb isotopic measurements were conducted with a MAT-261 thermal ionization mass spectrometer. First, to remove surface contamination, *c.* 50–80 mg of powder for each whole-rock sample was leached in acetone. Second, the samples were washed with distilled water and dried at 60 °C in an oven. Third, each whole-rock sample was dissolved in distilled HF + HNO_3 (150 °C, 168 h). Fourth, the Pb was separated on Teflon columns using an HBr–HCl wash with an elution procedure and then loaded with a mixture of Sigel and H_3PO_4 onto a single Re filament (1300 °C). The measured Pb isotope ratios were corrected by

https://doi.org/10.1017/S0016756821000479 Published online by Cambridge University Press

repeated analyses of the NBS-981 Pb standard. The total procedural blanks for Pb was were lower than 200 pg. In this study, the detailed operating conditions and analytical method were the same as those described by Xu *et al.* (2020).

5. Results

5.a. Zircon LA-ICP-MS U–Pb dating

Medium-grained granodiorite samples (EGX-1 and XSH-5) and porphyritic granite samples (EGX-2 and EGX-3) were selected for zircon U–Pb geochronology study. The results of zircon U–Pb dating are given in Table 1, and the corresponding CL images, concordia diagrams, weighted ages and chondrite-normalized rare earth element (REE) patterns of the zircon are shown in Figures 5, 6 and 7.

In the CL images, the characteristics of the zircon grains from the medium-grained granodiorite and porphyritic granite are similar. The zircons are columnar or short columnar, with good crystal shapes and clear edges and corners (80–250 μm long; length/width ratios of 1:1 to 3:2), and display clear oscillatory growth zoning in the CL images (Fig. 5). The U and Th contents and the Th/U ratios of the zircons are 131–1667 ppm, 53–1241 ppm and 0.40–0.87 (average value 0.63) for the granodiorite and 140–1732 ppm, 85–1282 ppm and 0.32–1.06 (average value 0.55) for the porphyritic granite, respectively, indicating that the zircons are of magmatic origin (Hoskin & Schaltegger, 2003).

The zircon grains collected from EGX-1 yield $^{206}Pb/^{238}U$ ages of 183–186 Ma, with a weighted mean $^{206}Pb/^{238}U$ age of 183.8 ± 1.4 Ma (2σ; $n = 18$; MSWD = 0.056; Fig. 6a). The zircon grains collected from XSH-5 yield $^{206}Pb/^{238}U$ ages of 178–184 Ma, with a weighted mean $^{206}Pb/^{238}U$ age of 181.9 ± 1.6 Ma (2σ; $n = 13$; MSWD = 0.34; Fig. 6b). However, there is one zircon with older $^{206}Pb/^{238}U$ ages of 197 Ma and 202 Ma in each sample (Fig. 5). These grains may be inherited or were captured by early magmatic events. The REE patterns (Fig. 7) of the medium-grained granodiorite and porphyritic granite are typically characterized by heavy REE (HREE) enrichment and light REE (LREE) depletion with distinct positive Ce anomalies and strongly negative Eu anomalies. Therefore, we believe that the granodiorite and porphyry granite are comagmatic and formed in the Early Jurassic (181.9–183.8 Ma).

In addition, the variation in crystallization temperature and oxygen fugacity of granodiorite and porphyritic granite with the trace element content in zircon was estimated using software developed by Li *et al.* (2019). On the basis of zircon trace element and whole-rock geochemical data, Ce^{4+}/Ce^{3+}, magmatic temperature and oxygen fugacity were calculated as functions of REE and Ti concentrations in zircons. Appropriate zircons with low La contents (<1 ppm) were selected for estimation to avoid the influence of mineral inclusions such as monazite in zircons (Zou *et al.* 2019). The estimated results are presented in Table 2. The granodiorite has high magmatic temperatures ranging from 790 °C to 891 °C (mean = 854 °C) and variable ΔFMQ values of −1.55 to +5.55 (mean = +1.82). Compared with the granodiorite, the porphyritic granite has a relatively lower crystallization temperature (697–813 °C; mean = 778 °C) and oxygen fugacity (ΔFMQ = −4.56 to +1.78; mean = −0.47).

5.b. Electron microprobe analysis of amphibole

Three amphibole crystals (seven analyses) from two granodiorite samples collected from the surface are Mg–hornblende in composition (Fig. 7c), and show little compositional variation in their major elements, with 47.97–49.70 wt % SiO_2, 0.52–0.97 wt % TiO_2, 5.54–6.26 wt % Al_2O_3, 15.84–16.71 wt % FeO, 11.58–12.22 wt % MgO and 10.70–1.22 wt % CaO (Table 3). The equations proposed by Ridolfi *et al.* (2010) were used to estimate the T, H_2O content and fO_2 of the magma from which amphiboles crystallized. The calculated temperatures and pressures of amphibole grains have narrow ranges of 732–772 °C (753 ± 18 °C) and 0.77–0.93 kbar (0.83 ± 0.09 kbar), respectively; therefore, we infer that these amphiboles crystallized at depths of 2.90–3.49 km (3.13 km; assuming conditions of lithostatic pressure with $\rho = 2.7\ g\ m^{-3}$) (Table 3). These computations were performed with the Geo-fO_2 software (Li *et al.* 2019).

5.c. Whole-rock geochemistry

The major and trace element concentrations of the seven medium-grained granodiorite and four porphyritic granite samples analysed in this study are presented in Table 4. The granodiorites have the following composition: SiO_2 = 62.02–65.73 wt %, Al_2O_3 = 14.82–16.99 wt %, K_2O = 3.07–4.54 wt %, and $Na_2O + K_2O$ = 7.40–8.31 wt %. Compared with the granodiorites, the porphyritic granite has higher concentrations of SiO_2 (72.09–73.94 wt %) and K_2O (4.13–5.10 wt %) and lower concentrations of Al_2O_3 (13.62–14.73 wt %). In the plot of the total alkalis vs SiO_2 (TAS) diagram, the granodiorite samples plot on the boundary lines separating the quartz monzogranite, diorite and granodiorite fields, and the porphyritic granite plots within the granite field (Fig. 8a; Middlemost, 1994) and is classified as subalkaline (Irvine & Baragar, 1971). The granodiorite and porphyritic granite samples are classified as potassic suites based on the K_2O vs Na_2O diagram (Fig. 8b; Middlemost, 1972). In the SiO_2 vs K_2O diagram (Fig. 8C; Peccerillo & Taylor, 1976), most samples plot in the high-K calc-alkaline series field, and a few samples plot in the shoshonite series. Their A/CNK and A/NK values range from 0.86 to 0.97 and 1.42 to1.79, respectively, falling in the metaluminous and weakly peraluminous regions (Fig. 8d; Maniar & Piccoli, 1989). In addition, the granodiorite samples plot on the junction of Fe, Cu and Zn deposits in the TAS diagram (Fig. 8a), SiO_2 vs K_2O diagram (Fig. 8c) and A/CNK vs A/NK diagram (Fig. 8d).

The granodiorite samples and porphyritic granite have high contents of large-ion lithophile elements (LILEs; such as Rb and Ba) and LREEs and are relatively depleted in high field strength elements (HFSEs; Nb, Ta, Hf and Th). These rocks are rich in LREEs but depleted in HREEs (Fig. 8e; Boynton, 1984). The granodiorite samples are moderately fractionated, yielding LREE/HREE ratios of 6.85–10.95 (with a mean of 9.05), and clearly negative Eu anomalies (δEu = 0.38–0.66, with a mean of 0.51). In comparison, the porphyritic granite samples have higher degrees of fractionation between LREEs and HREEs, with LREE/HREE ratios of 7.03–10.56 (with a mean of 9.28) and strongly negative Eu anomalies (δEu = 0.23–0.28, with a mean of 0.26). In a primitive mantle-normalized trace element spider diagram (Fig. 8f; Sun & McDonough, 1989), the samples are enriched in Rb, Th, U and LREEs and depleted in Sr and HFSEs, such as Nb, Ta, P and Ti.

5.d. Zircon Lu–Hf isotopic data

The results of the Lu–Hf isotope analysis of the granodiorite (EGX-1, XSH-5) and porphyry granite (EGX-20) zircon U–Pb spots are listed in Table 5. The 29 magmatic zircons from the granodiorite, all of which yield similar ages (178.0–186.4 Ma), have

https://doi.org/10.1017/S0016756821000479 Published online by Cambridge University Press

Table 1. LA-ICP-MS zircon U–Pb of granodiorite (EGX-1 and XSH-5) and porphyritic granite (EGX-2 and EGX-3) from the Ergu Fe–Zn polymetallic deposit

	Element (ppm)				Isotope ratio						Apparent age (Ma)					
Spot	Pb*	Th	U	Th/U	$^{207}Pb/^{206}Pb$	1σ	$^{207}Pb/^{235}U$	1σ	$^{206}Pb/^{238}U$	1σ	$^{207}Pb/^{206}Pb$	1σ	$^{207}Pb/^{235}U$	1σ	$^{206}Pb/^{238}U$	1σ
EGX-1, granodiorite, 18 spots (except point 10), weighted mean age = 183.8 ± 1.4 Ma, MSWD = 0.20																
1	27	470	685	0.69	0.05029	0.00180	0.19968	0.00684	0.02880	0.00040	208	81	185	6	183	3
2	13	178	353	0.50	0.04974	0.00199	0.19946	0.00766	0.02908	0.00041	183	90	185	6	185	3
3	19	359	462	0.78	0.04943	0.00235	0.19638	0.00898	0.02882	0.00046	168	107	182	8	183	3
4	9	157	246	0.64	0.04997	0.00569	0.19946	0.02204	0.02895	0.00088	193	245	185	19	184	5
5	12	163	313	0.52	0.04956	0.00188	0.19774	0.00720	0.02894	0.00041	174	86	183	6	184	3
6	12	166	316	0.52	0.04972	0.00218	0.19846	0.00838	0.02895	0.00042	182	99	184	7	184	3
7	11	189	290	0.65	0.04976	0.00264	0.19757	0.01014	0.02879	0.00047	184	119	183	9	183	3
8	17	308	429	0.72	0.05065	0.00316	0.20108	0.01204	0.02879	0.00058	225	138	186	10	183	4
9	65	1241	1667	0.74	0.04951	0.00097	0.19749	0.00366	0.02893	0.00030	172	45	183	3	184	2
10	11	201	282	0.71	0.04997	0.00404	0.21360	0.01675	0.03100	0.00069	193	178	197	14	197	4
11	8	123	234	0.53	0.04866	0.00427	0.19690	0.01678	0.02934	0.00069	132	194	183	14	186	4
12	13	180	356	0.50	0.04954	0.00202	0.19759	0.00780	0.02893	0.00039	173	93	183	7	184	2
13	14	185	343	0.54	0.04949	0.00257	0.19638	0.00979	0.02878	0.00050	171	117	182	8	183	3
14	11	204	295	0.69	0.04987	0.00308	0.19915	0.01193	0.02896	0.00051	189	138	184	10	184	3
15	39	618	1007	0.61	0.04958	0.00134	0.19771	0.00509	0.02892	0.00034	175	62	183	4	184	2
16	7	151	201	0.75	0.04979	0.00449	0.19732	0.01728	0.02874	0.00069	185	197	183	15	183	4
17	5	58	126	0.46	0.05010	0.00473	0.19978	0.01848	0.02892	0.00061	200	206	185	16	184	4
18	6	100	155	0.65	0.04973	0.00391	0.19881	0.01518	0.02899	0.00060	183	173	184	13	184	4
19	17	386	445	0.87	0.05000	0.00253	0.19852	0.00969	0.02880	0.00046	195	114	184	8	183	3
XSH-5, granodiorite, 13 spots (except point 6), weighted mean age = 181.9 ± 1.6 Ma, MSWD = 0.34																
1	18	77	156	0.49	0.05029	0.00275	0.19857	0.01059	0.02864	0.00053	208	89	184	9	182	3
2	26	154	216	0.71	0.04974	0.00261	0.19652	0.01007	0.02865	0.00052	183	85	182	9	182	3
3	34	168	292	0.58	0.05108	0.00245	0.20404	0.00955	0.02897	0.00051	244	75	189	8	184	3
4	19	106	167	0.64	0.05223	0.00276	0.20764	0.01070	0.02883	0.00053	295	84	192	9	183	3
5	15	53	131	0.40	0.04964	0.00276	0.19552	0.01063	0.02856	0.00053	178	91	181	9	182	3
6	18	93	155	0.60	0.05095	0.00370	0.22342	0.01575	0.03180	0.00072	239	120	205	13	202	4
7	24	106	212	0.50	0.05018	0.00248	0.19337	0.00934	0.02795	0.00049	203	79	180	8	178	3
8	32	223	278	0.80	0.05186	0.00220	0.20324	0.00847	0.02842	0.00047	279	65	188	7	181	3
9	19	99	163	0.61	0.04717	0.00268	0.18746	0.01041	0.02882	0.00054	58	87	174	9	183	3
10	32	160	284	0.56	0.05109	0.00210	0.19968	0.00805	0.02835	0.00046	245	63	185	7	180	3
11	35	231	308	0.75	0.05183	0.00203	0.20679	0.00795	0.02894	0.00046	278	59	191	7	184	3
12	21	111	182	0.61	0.05297	0.00266	0.21085	0.01031	0.02887	0.00052	328	78	194	9	183	3
13	22	105	190	0.55	0.05195	0.00263	0.20581	0.01017	0.02873	0.00052	283	80	190	9	183	3
14	36	251	326	0.77	0.05372	0.00203	0.20924	0.00778	0.02825	0.00045	359	55	193	7	180	3
EGX-2, porphyritic granite, 14 spots (except point 8), weighted mean age = 182.7 ± 1.8 Ma, MSWD = 0.21																
1	35	149	301	0.50	0.05371	0.00259	0.21400	0.01004	0.02890	0.00051	359	74	197	8	184	3
2	26	96	220	0.44	0.05110	0.00391	0.20176	0.01497	0.02863	0.00069	245	125	187	13	182	4
3	22	138	185	0.74	0.05053	0.00250	0.20162	0.00976	0.02894	0.00051	219	79	186	8	184	3
4	25	108	214	0.50	0.04911	0.00234	0.19419	0.00906	0.02868	0.00049	153	77	180	8	182	3
5	45	310	384	0.81	0.05169	0.00247	0.20296	0.00947	0.02848	0.00050	272	75	188	8	181	3
6	28	90	233	0.39	0.05133	0.00406	0.20802	0.01594	0.02939	0.00072	256	129	192	13	187	5
7	16	85	140	0.60	0.04967	0.00317	0.19524	0.01215	0.02851	0.00058	180	105	181	10	181	4
8	215	617	1953	0.32	0.05083	0.00145	0.22111	0.00627	0.03155	0.00044	233	40	203	5	200	3

(*Continued*)

https://doi.org/10.1017/S0016756821000479 Published online by Cambridge University Press

Table 1. (*Continued*)

	Element (ppm)				Isotope ratio						Apparent age (Ma)					
Spot	Pb*	Th	U	Th/U	$^{207}Pb/^{206}Pb$	1σ	$^{207}Pb/^{235}U$	1σ	$^{206}Pb/^{238}U$	1σ	$^{207}Pb/^{206}Pb$	1σ	$^{207}Pb/^{235}U$	1σ	$^{206}Pb/^{238}U$	1σ
9	25	126	210	0.60	0.04955	0.00205	0.19791	0.00801	0.02897	0.00047	174	64	183	7	184	3
10	43	227	363	0.62	0.05067	0.00336	0.22066	0.01421	0.03158	0.00068	226	108	202	12	200	4
11	23	91	194	0.47	0.05099	0.00249	0.20166	0.00961	0.02868	0.00050	240	78	187	8	182	3
12	41	455	972	0.47	0.05026	0.00368	0.19873	0.01413	0.02868	0.00066	207	119	184	12	182	4
13	45	287	386	0.74	0.04986	0.00355	0.19810	0.01368	0.02881	0.00065	188	115	184	12	183	4
14	39	127	343	0.37	0.04989	0.00352	0.20035	0.01370	0.02913	0.00065	190	114	185	12	185	4
15	62	550	518	1.06	0.05101	0.00206	0.20194	0.00800	0.02871	0.00046	241	62	187	7	182	3
16	111	115	319	0.36	0.05078	0.00148	0.19975	0.00579	0.02853	0.00040	231	41	185	5	181	3
EGX-3, porphyritic granite, 15 spots (except point 9), weighted mean age = 182.7 ± 1.4 Ma, MSWD = 0.35																
1	45	164	389	0.42	0.04908	0.00175	0.19792	0.00694	0.02925	0.00045	152	53	183	6	186	3
2	38	149	333	0.45	0.05080	0.00333	0.20130	0.01279	0.02873	0.00063	232	106	186	11	183	4
3	107	536	903	0.59	0.04976	0.00113	0.19713	0.00452	0.02873	0.00039	184	29	183	4	183	2
4	37	197	317	0.62	0.05039	0.00198	0.20213	0.00780	0.02908	0.00047	213	59	187	7	185	3
5	24	114	210	0.54	0.05110	0.00228	0.20082	0.00874	0.02849	0.00049	245	68	186	7	181	3
6	55	295	484	0.61	0.05380	0.00171	0.21028	0.00659	0.02833	0.00042	363	44	194	6	180	3
7	46	157	406	0.39	0.04975	0.00179	0.19547	0.00691	0.02848	0.00044	183	54	181	6	181	3
8	30	193	254	0.76	0.04958	0.00196	0.19885	0.00772	0.02907	0.00047	175	60	184	7	185	3
9	212	1282	1732	0.74	0.05129	0.00101	0.22605	0.00459	0.03195	0.00042	254	24	207	4	203	3
10	34	130	299	0.43	0.05049	0.00267	0.19832	0.01020	0.02848	0.00053	218	84	184	9	181	3
11	32	122	277	0.44	0.04976	0.00275	0.19849	0.01070	0.02892	0.00055	184	90	184	9	184	3
12	39	239	336	0.71	0.04975	0.00173	0.19653	0.00675	0.02864	0.00043	183	52	182	6	182	3
13	198	531	1659	0.32	0.05195	0.00097	0.20675	0.00401	0.02886	0.00037	283	23	191	3	183	2
14	66	262	568	0.46	0.05078	0.00148	0.19975	0.00579	0.02853	0.00040	231	41	185	5	181	3
15	40	195	344	0.57	0.05101	0.00206	0.20194	0.00800	0.02871	0.00046	241	62	187	7	182	3
16	56	227	482	0.47	0.05026	0.00368	0.19873	0.01413	0.02868	0.00066	207	119	184	12	182	4

initial $^{176}Hf/^{177}Hf$ ratios of 0.282656–0.282804, $\epsilon_{Hf}(t)$ values of −0.5 to +5.1 and T_{DM2} ages ranging from 902 to 1630 Ma. Two zircons with ages of 196.8 Ma (EGX-1-10) and 202 Ma (XSH-5-06) have initial $^{176}Hf/^{177}Hf$ ratios of 0.282679–0.282829, with $\epsilon_{Hf}(t)$ of +1.1 to +6.2 and T_{DM2} ages of 841 to 1573 Ma, respectively. The nine magmatic zircons from the porphyry granite, all of which yield ages of 181 to 187 Ma, have initial $^{176}Hf/^{177}Hf$ ratios of 0.282684–0.282827, $\epsilon_{Hf}(t)$ values of +0.73 to +5.86 and T_{DM2} ages of 850 to 1174 Ma. One zircon with an age of 200 Ma (EGX-2-12) has initial $^{176}Hf/^{177}Hf$ ratios of 0.282750, with $\epsilon_{Hf}(t)$ and T_{DM2} values of +3.61 and 1006 Ma, respectively. The Lu–Hf isotopic characteristics of the granodiorite and porphyry granite are similar to those of typical porphyry–skarn deposits in NE China. The analysed zircons plot in the field formed by Phanerozoic igneous rocks in the eastern CAOB in the plot of age vs $\epsilon_{Hf}(t)$ (Fig. 9a, b) and between depleted mantle and young lower crust in the plot of age vs $^{176}Hf/^{177}Hf$ (Fig. 9c, d).

5.e. Sr–Nd–Pb isotopes

The whole-rock Sr–Nd isotopic compositions of the granodiorites are presented in Table 6 and plotted in Figure 10. The four granodiorite samples have whole-rock initial $(^{87}Sr/^{86}Sr)_i$ ratios from 0.7060 to 0.7090 and calculated $\epsilon Nd(t)$ values of −1.7 to −1.4, corresponding to depleted mantle model ages (T_{DM2}) of 1078–1108 Ma. All these rocks have similar Sr–Nd isotopic compositions within the range of ore-related granitoids associated with typical porphyry–skarn deposits in NE China and in the CAOB reported by previous studies (Fig. 10a, b, c; Wu *et al.* 2000, 2003). The Ergu granodiorites also define a restricted range of radiogenic Pb isotopic compositions with $(^{206}Pb/^{204}Pb)_t$, $(^{207}Pb/^{204}Pb)_t$ and $(^{208}Pb/^{204}Pb)_t$ values of 18.3944–18.7603, 15.5825–15.6040 and 38.1262–38.4679 (Table 6), respectively. In the $^{207}Pb/^{204}Pb$ vs $^{206}Pb/^{204}Pb$ diagram (Fig. 10d), the granodiorite samples plot within the field of the lower crust.

6. Discussion

6.a. Ages of magmatism and mineralization

In the field of hydrothermal deposit research, it is very important to accurately define the timing of diagenesis and mineralization when discussing the genesis and metallogenic dynamic background and when providing prospecting guidance. To date, numerous studies have collected geochronological data on hydrothermal deposits in the Lesser Xing'an Range, and it is widely believed that the

https://doi.org/10.1017/S0016756821000479 Published online by Cambridge University Press

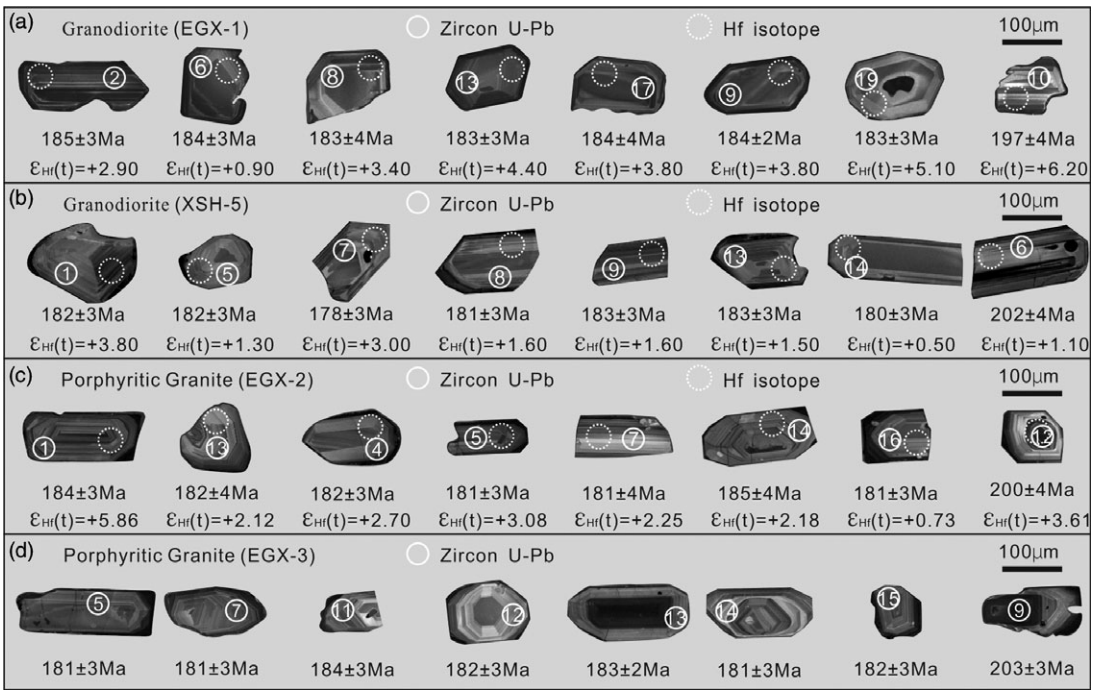

Fig. 5. Cathodoluminescence (CL) images of representative analysed zircons from granodiorite (a, b) and porphyritic granite (c, d) of the Ergu Fe–Zn polymetallic deposit. Full line represents U–Pb age analytical spot; dashed line represents Hf isotope analytical spot.

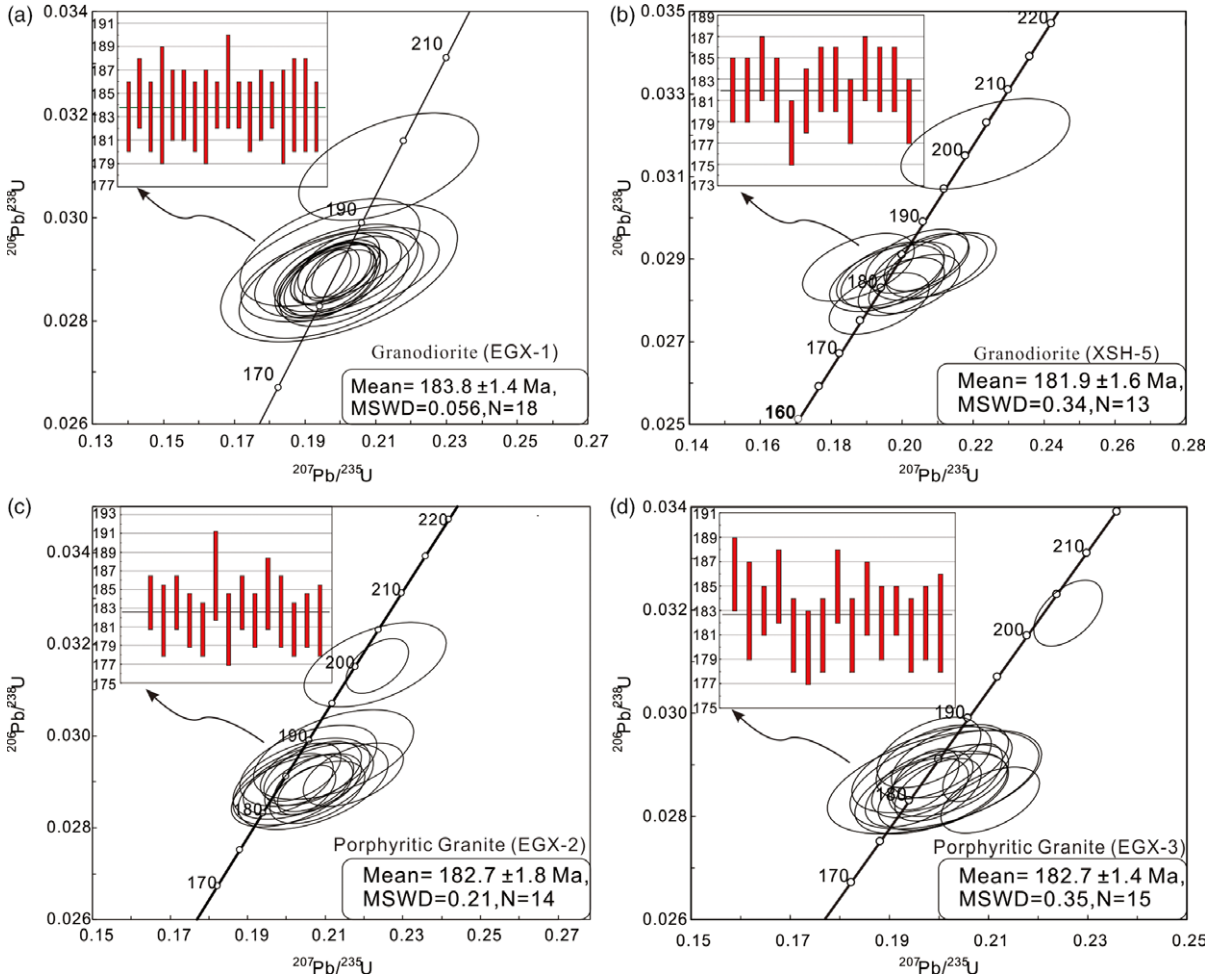

Fig. 6. (Colour online) Concordia diagrams of zircon U–Pb ages and the weighted mean diagrams for granodiorite (a, b) and porphyritic granite (c, d) of the Ergu Fe–Zn polymetallic deposit.

https://doi.org/10.1017/S0016756821000479 Published online by Cambridge University Press

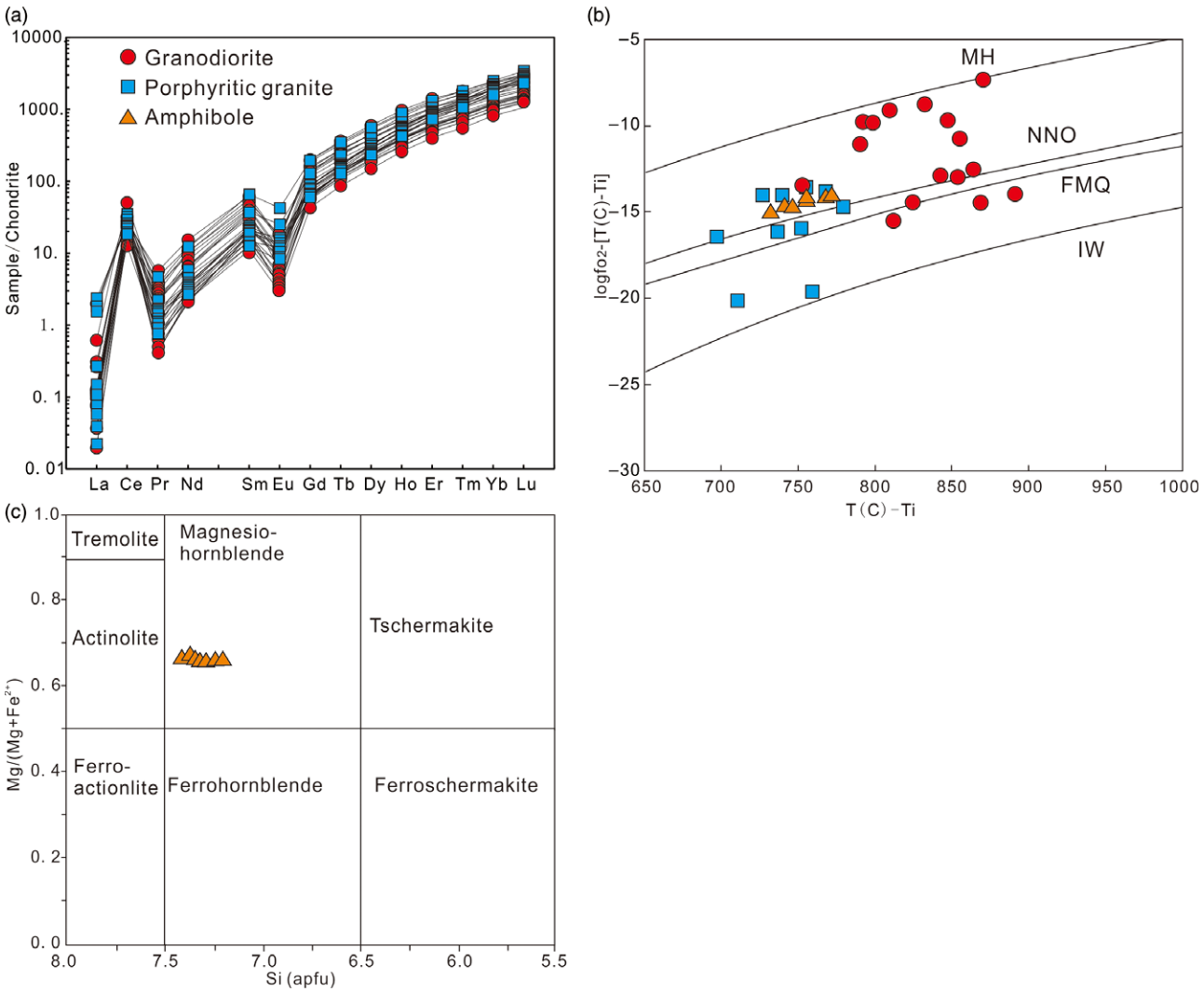

Fig. 7. (Colour online) Chondrite-normalized REE patterns of zircon grains (a), magma oxygen fugacity (fo_2) of the granodiorite, porphyritic granite and amphibole of granodiorite in the Ergu deposit (b), and classifications and compositions of amphiboles (c). MH = magnetite–hematite buffer; NNO = Ni–NiO buffer; FMQ = fayalite–magnetite–quartz buffer; IW = iron–wustite buffer. The calculation method of $lgfo_2$ and T (Ti-in-zircon thermometer) is based on Ferry & Watson (2007) and Qiu *et al.* (2013).

porphyry and skarn deposits formed in the Early–Middle Jurassic, especially within the range 175–186.8 Ma (Fig. 11; Table 7), indicating that the large-scale skarn and porphyry deposits in the study area formed in the Early Jurassic (Sun *et al.* 2004; Wu *et al.* 2011; Xu *et al.* 2013).

As described above, the zircon grains analysed in this study are euhedral–subhedral and exhibit oscillatory growth zoning (Fig. 5) and high Th/U ratios, indicating a magmatic origin and suggesting that the zircon U–Pb ages represent the crystallization ages of their host rocks. Our new age data for the medium-grained granodiorites and porphyritic granites are 181.9–183.8 Ma and 182.7 Ma, respectively. These ages are consistent with the geochronological characteristics of Early Jurassic magmatism in the Lesser Xing'an Range. Moreover, Ouyang & Che (2016) found that the ^{40}Ar–^{39}Ar age of phlogopite in the altered rock of the Ergu deposit is 181.0 ± 4.2 Ma. These findings, combined with field geological observations, confirm not only that the magmatism related to the mineralization was granodioritic magma but also that the diagenesis and mineralization age of the Ergu deposit is in accordance with those of the regional large-scale skarn deposits and porphyry deposits that formed in the Early Jurassic.

6.b. Petrogenesis

6.b.1. Rock types and differentiation characteristics

Evaluating the genetic type of granitoids is significant for revealing the magma source region, magmatic process, deep geodynamic process and their constraints on mineralization (Pearce *et al.* 1984; Sylvester, 1998; Barbarin, 1999). Since Chappell & White (1974) proposed dividing granites into S-type and I-type granites according to their sources, it has been generally accepted that the granites can be divided into four types: A-type, I-type, S-type and M-type, according to the nature of their protoliths (Pitcher, 1997).

The petrographic characteristics of the granodiorite in the Ergu deposit show that the granodiorite and porphyritic granite do not contain the special Al-rich minerals (Chappell, 1999) (such as muscovite and cordierite) present in S-type granite and do not contain the alkali mafic minerals (such as riebeckite, sodic pyroxene and annite) present in A-type granite. The granodiorite and porphyritic granite are metaluminous with A/CNK values ranging from 0.86 to 1.10 and are distinguishable from the typical S-type granites which possess strongly peraluminous affinity with A/CNK values much higher than 1.1 (Chappell & White, 2001). Moreover, in the plot of A/CNK vs A/NK (Fig. 8d), most samples plot within

https://doi.org/10.1017/S0016756821000479 Published online by Cambridge University Press

Table 2. Zircon grains trace elements of granodiorite (EGX-1) and porphyritic granite (EGX-2) from the Ergu Fe–Zn polymetallic deposit

Element	Ti	La	Ce	Pr	Nd	Sm	Eu	Gd	Tb	Dy	Ho	Er
Unit	ppm	ppm	ppm	ppm	ppm	ppm	ppm	ppm	ppm	ppm	ppm	ppm
Granodiorite (EGX-1)												
1	19.56	0.0047	14.46	0.0411	1.00	2.75	0.40	12.14	4.44	51.00	18.19	83.37
2	11.00	0.0185	17.19	0.0640	1.12	2.39	0.22	12.53	4.53	53.27	20.19	91.31
3	19.00	0.0740	16.93	0.5440	7.33	9.75	0.94	41.97	13.89	156.64	56.55	241.07
4	16.97	0.0230	12.36	0.2030	3.07	4.88	0.55	20.86	6.84	75.83	27.75	117.78
5	9.45	0.0300	14.59	0.0594	1.22	2.91	0.19	13.91	4.92	60.71	22.27	101.56
6	10.24	0.0250	15.38	0.0470	0.96	2.91	0.27	15.24	5.31	62.34	23.66	106.22
7	15.37	0.0240	14.92	0.2130	3.17	5.21	0.57	23.97	7.80	87.52	31.25	136.41
8	11.63	0.0280	19.98	0.3570	5.69	8.87	0.90	39.29	12.64	139.47	49.83	212.55
9	18.09	0.0311	14.86	0.2730	4.89	8.02	1.07	33.64	10.59	118.32	42.29	180.61
10	17.17	0.0088	11.20	0.1031	1.65	3.42	0.54	17.51	5.60	62.72	22.75	101.78
11	14.03	0.0215	13.43	0.0400	1.07	2.01	0.22	11.79	4.12	48.53	17.76	81.71
12	9.62	0.0250	17.52	0.0393	1.16	2.35	0.24	13.34	4.90	57.22	22.03	98.53
14	13.07	0.0240	14.89	0.2130	3.75	6.33	0.60	28.70	9.12	102.83	36.83	156.70
16	23.24	0.0310	11.60	0.3160	5.00	7.21	1.05	29.99	9.51	100.70	35.69	146.47
17	16.03	0.0251	8.12	0.0700	1.06	1.72	0.17	9.04	3.32	38.84	15.05	68.60
18	18.53	0.0177	9.64	0.1360	2.41	3.84	0.50	16.75	5.41	61.91	22.33	95.28
Porphyritic granite (EGX-2)												
2	6.35	0.0354	20.23	0.2120	2.74	5.66	1.46	26.36	8.62	99.79	37.40	173.71
4	3.46	0.0092	15.35	0.0898	1.37	3.12	0.72	16.50	5.83	73.51	29.03	139.60
5	6.56	0.0640	19.59	0.1157	1.73	3.64	0.83	18.07	6.46	82.05	32.30	149.61
7	5.57	0.0181	15.87	0.0721	1.25	3.22	0.58	18.12	6.08	82.34	31.20	147.06
8	4.04	0.0420	20.69	0.2770	4.47	8.37	1.39	34.21	11.26	131.68	49.17	220.27
10	7.48	0.0053	10.83	0.1240	1.73	2.19	0.71	12.32	4.90	59.36	25.37	128.06
11	5.39	0.0256	11.92	0.0964	1.84	3.08	0.77	12.53	5.03	65.59	25.44	121.23
13	6.83	0.0152	12.01	0.3200	4.84	6.65	1.95	28.82	9.36	104.78	38.51	169.98

(*Continued*)

Table 2. (*Continued*)

Element	Ti	La	Ce	Pr	Nd	Sm	Eu	Gd	Tb	Dy	Ho	Er
Unit	ppm	ppm	ppm	ppm	ppm	ppm	ppm	ppm	ppm	ppm	ppm	ppm
14	8.40	0.0137	10.88	0.0865	2.11	3.17	0.95	15.97	5.41	71.51	28.32	136.12
16	6.35	0.0354	20.23	0.2120	2.74	5.66	1.46	26.36	8.62	99.79	37.40	173.71

Element	Tm	Yb	Lu	Y	Hf	Th	U	T			log(f_{O2})	ΔFMQ
Unit	ppm	ppm	ppm	ppm	ppm	ppm	ppm	°C	Ce^{4+}/Ce^{3+}	Eu_N/Eu_{N^*}	Trail *et al.* (2012)	
Granodiorite (EGX-1)												
1	17.4	169	33.3	579	9775	105	190	870	56.2	0.42	−7.33	5.55
2	19.3	185	35.8	623	9293	165	324	809	75.1	0.24	−9.10	5.00
3	47.2	424	79.60	1662	8065	354	455	869	8.04	0.28	−14.5	−1.55
4	24.2	224	42.8	829	8036	151	238	854	14.9	0.33	−13.0	0.22
5	21.5	207	40.2	686	9387	141	278	790	55.9	0.19	−11.1	3.45
6	22.7	214	41.8	724	9351	162	301	799	70.4	0.25	−9.82	4.52
7	27.3	250	47.2	939	8683	182	283	842	17.6	0.31	−12.9	0.54
8	41.7	379	70.1	1458	9218	303	421	812	12.3	0.29	−15.5	−1.46
9	36.3	327	60.3	1261	9308	231	308	861	9.60	0.40	−14.0	−0.98
10	21.0	201	38.7	702	9254	111	182	855	25.6	0.42	−10.8	2.35
11	17.5	166	31.9	556	9081	120	227	832	62.1	0.27	−8.75	4.87
12	21.1	200	39.1	667	9684	174	344	792	78.1	0.26	−9.77	4.71
14	31.4	288	53.5	1088	8955	191	278	825	14.1	0.27	−14.4	−0.65
16	29.1	266	49.0	1030	8149	148	195	891	6.99	0.43	−14.0	−1.54
17	14.5	143	27.5	461	8781	56.4	123	847	40.1	0.26	−9.68	3.64
18	19.5	184	34.5	671	7918	97.4	150	864	14.9	0.38	−12.5	0.47
Porphyritic granite (EGX-2)												
2	37.77	379.68	79.34	1167.50	8622.38	196.81	316.57	751.10	22.73	1.41	−15.94	−0.52
4	31.58	326.32	67.43	915.98	8483.73	121.94	277.24	696.53	43.62	1.19	−16.43	0.36
5	32.78	330.49	67.79	1013.17	7876.74	238.84	336.01	754.19	41.82	1.21	−13.57	1.78
7	31.59	319.44	65.15	991.77	9601.80	262.08	567.82	738.80	45.43	0.90	−14.03	1.68
8	46.94	453.21	91.82	1478.69	8263.65	195.22	343.58	709.90	12.81	0.97	−20.10	−3.66
10	29.00	302.87	66.76	835.22	7996.15	96.33	220.17	766.88	32.98	1.61	−13.82	1.23
11	27.56	277.15	58.62	815.16	8171.94	107.59	213.59	735.77	26.66	1.45	−16.13	−0.35
13	36.25	355.35	74.42	1194.77	7303.63	125.87	209.97	758.06	6.72	1.66	−19.81	−4.56
14	30.19	298.02	63.42	901.06	7157.09	90.72	194.37	778.36	20.98	1.58	−14.91	−0.12
16	37.77	379.68	79.34	1167.50	8622.38	196.81	316.57	751.10	22.73	1.41	−15.94	−0.52

Table 3. Composition of amphibole from the Ergu granodiorites

Sample	EGX-1				XSH-5		
Grain	EGX-1-1	EGX-1-2	EGX-1-3	EGX-1-4	XSH-5-1	XSH-5-2	XSH-5-3
SiO_2	48.7	49.4	49.7	49.0	48.9	48.5	48.0
TiO_2	0.71	0.52	0.55	0.69	0.53	0.88	0.97
Al_2O_3	5.90	5.54	5.56	5.88	5.61	6.02	6.26
Cr_2O_3	0.00	0.03	0.00	0.00	0.00	0.00	0.03
FeO	16.3	16.2	16.4	16.3	16.7	15.8	15.9
MnO	0.29	0.33	0.31	0.36	0.34	0.31	0.38
MgO	12.0	12.1	11.6	11.6	12.2	12.1	12.1
CaO	11.1	11.1	10.9	11.0	10.7	11.2	10.9
Na_2O	1.02	1.00	0.92	0.97	0.87	1.15	1.18
K_2O	0.49	0.48	0.50	0.55	0.58	0.65	0.55
Total	96.51	96.66	96.43	96.22	96.46	96.67	96.17
Si	7.32	7.41	7.48	7.39	7.35	7.28	7.24
Al^{IV}	0.80	0.71	0.65	0.73	0.81	0.83	0.89
Al^{VI}	0.23	0.25	0.32	0.30	0.16	0.23	0.20
Ti	0.08	0.06	0.06	0.08	0.06	0.10	0.11
Fe^{3+}	0.51	0.47	0.41	0.41	0.80	0.39	0.57
Fe^{2+}	1.50	1.53	1.62	1.61	1.26	1.57	1.40
Mn	0.04	0.04	0.04	0.05	0.04	0.04	0.05
Mg	2.64	2.65	2.56	2.56	2.68	2.68	2.67
Ca	1.76	1.75	1.72	1.74	1.69	1.78	1.73
Na	0.24	0.25	0.26	0.26	0.25	0.22	0.27
K	0.09	0.09	0.09	0.10	0.11	0.12	0.10
T (°C)	755	741	732	746	755	768	772
P (MPa)	0.84	0.77	0.77	0.84	0.78	0.87	0.93
Uncertainty (max. error)	0.09	0.08	0.09	0.09	0.09	0.10	0.10
Oceanic depth (km)	2.97	2.71	2.73	2.97	2.74	3.07	3.26
Continental depth (km)	3.18	2.90	2.92	3.18	2.94	3.29	3.49
ΔFMQ	1.76	1.83	1.69	1.63	1.97	1.68	1.70
ΔHM	−4.11	−4.06	−4.21	−4.24	−3.90	−4.17	−4.13
$logfO_2$	−14.28	−14.57	−14.94	−14.63	−14.07	−14.05	−13.92
Uncertainty (σ_{est})	0.40	0.40	0.40	0.40	0.40	0.40	0.40
H_2O melt (wt %)	5.82	5.80	6.17	6.07	5.23	5.25	5.52
Uncertainty*	0.40	0.40	0.40	0.40	0.40	0.40	0.40

*The structural formulae of the amphibolite were calculated on the basis of 23 oxygen atoms.

the area of the I-type granite area instead of the S-type granite area. Moreover, the decreasing P_2O_5 concentration with increasing SiO_2 concentration in the Ergu samples (Fig. 12a) indicates that the Ergu intrusions are I-type granite. Chappell & White (1992) pointed out that Th concentrations reveal a positive correlation with Rb in I-type granites and opposition in S-type granites. Therefore, the Th/Rb value can be used to distinguish S-type granite from I-type granite. Th concentrations increase with increasing Rb contents in Ergu intrusions (Fig. 12b), which can also exclude the characteristics of S-type granites. This conclusion is also supported by the FeO^t/Mg ratios (1.90–7.27) and MgO contents (0.29–2.98 %) of these intrusions. In contrast, typical A-type granites generally contain higher FeO^t/Mg ratios (10.87–64.00; Sun *et al.* 2004) and lower MgO contents (MgO wt % < 0.1 %; Whalen *et al.* 1987). Additionally, it is noteworthy that the 10 000 × Ga/Al values (0.95–2.68; mean of 2.38) of these granodiorites and porphyritic granite are below those of typical A-type granites (Whalen *et al.* 1987), further confirming their I-type affinity (Fig. 12c–f).

Although the granodiorite and porphyry granite are I-type granite, they have different major and trace element characteristics, which indicates that they have undergone different degrees of fractional crystallization. In terms of the FeO^t/Mg ratio, the

https://doi.org/10.1017/S0016756821000479 Published online by Cambridge University Press

Table 4. Whole-rock geochemical data of intrusions from the Ergu Fe–Zn polymetallic deposit (major elements wt %; trace elements ppm)

Rock type	Granodiorite							Porphyritic granite			
Sample No.	EGX-1a	EGX-1b	EGD-1a	EGD-1b	XSH-5a	XSH-5b	XSH-5c	EGX-2a	EGX-2b	EGX-3a	EGX-3b
SiO_2	62.02	62.10	63.51	64.71	65.73	64.67	64.51	72.09	72.23	73.53	73.94
Al_2O_3	16.20	15.93	16.18	16.99	14.82	15.16	15.38	14.73	14.30	13.62	13.68
Fe_2O_3	1.22	1.29	1.08	0.76	1.68	3.18	4.12	0.33	0.39	0.98	0.53
FeO	4.60	4.69	4.22	3.24	5.38	4.37	3.39	1.20	1.37	1.14	1.60
MgO	2.93	2.98	2.17	1.68	2.13	2.28	2.02	0.37	0.41	0.31	0.29
CaO	5.14	5.22	3.53	3.67	3.32	3.46	3.64	1.27	1.25	0.78	0.88
Na_2O	3.39	3.43	3.55	4.10	2.97	3.06	3.64	4.38	3.95	3.78	3.87
K_2O	3.22	3.07	4.44	3.82	4.54	4.30	3.78	4.73	5.10	4.80	4.13
MnO	0.11	0.11	0.08	0.06	0.10	0.11	0.11	0.04	0.04	0.04	0.05
TiO_2	0.94	0.95	1.04	0.80	0.81	0.85	1.09	0.26	0.22	0.20	0.19
P_2O_5	0.23	0.23	0.20	0.16	0.27	0.29	0.31	0.08	0.07	0.06	0.06
Lol	2.01	1.78	1.52	1.36	0.50	0.63	0.53	0.46	0.61	0.77	0.74
Total	99.79	99.80	99.75	99.79	99.65	99.62	99.86	99.94	99.94	100.00	99.96
TFeO	5.57	5.73	5.09	3.86	6.75	7.08	6.95	1.50	1.72	2.02	2.08
$K_2O + Na_2O$	6.61	6.50	7.99	7.93	7.52	7.36	7.41	9.11	9.05	8.58	8.00
A/NK	1.79	1.78	1.52	1.56	1.42	1.48	1.46	1.19	1.19	1.19	1.26
A/CNK	0.88	0.86	0.95	0.97	0.90	0.92	0.89	1.00	1.00	1.06	1.10
Mg#	48.03	47.83	42.94	43.45	35.67	39.18	39.37	30.86	30.08	21.37	19.84
DI	61.15	60.93	69.76	71.86	71.68	70.54	70.31	90.23	89.93	91.80	90.29
Li	23.91	34.68	59.64	45.67	41.60	52.60	50.40	17.30	17.80	20.10	21.60
Be	0.87	2.78	2.85	3.78	3.15	2.96	3.55	5.79	5.31	4.06	3.88
Rb	40.02	164.70	302.30	249.40	207.00	245.00	248.00	259.00	263.00	269.00	232.00
Ba	159.42	755.10	1103.56	940.94	637.00	669.00	667.00	407.00	370.00	390.00	334.00
Sr	866.11	541.69	375.51	410.22	264.00	271.00	282.00	170.00	156.00	104.00	128.00
Zr	243.67	247.51	392.11	298.68	389.00	460.00	280.00	223.00	209.00	227.00	226.00
Nb	5.79	11.19	18.04	16.53	15.70	16.10	20.50	21.60	17.20	16.50	14.40
Hf	7.11	11.64	13.36	10.55	10.90	12.50	7.51	6.74	6.00	5.61	6.75
Ta	0.36	0.35	1.24	1.22	1.63	1.49	2.23	2.90	2.29	1.80	1.27
Th	4.72	21.85	24.01	22.81	28.60	29.10	38.00	36.10	29.70	30.90	34.70
U	2.58	8.75	7.85	9.54	9.79	9.71	17.80	9.34	7.88	5.06	5.80
V	62.61	126.52	97.10	75.50	95.60	112.00	95.30	17.50	25.30	21.30	18.80
Cr	41.88	44.86	26.95	23.17	31.30	38.10	23.30	263.00	262.00	275.00	272.00
Co	10.98	16.91	12.57	9.74	14.80	13.60	12.60	1.33	1.65	2.08	1.69
Ni	27.94	18.74	11.23	8.90	14.30	16.10	11.20	5.60	5.50	5.89	7.86
Ga	8.15	21.87	22.90	24.01	20.00	21.50	21.20	19.20	19.50	17.50	17.40
Tl	0.41	1.74	1.91	1.41	1.79	1.98	1.68	1.33	1.38	2.16	1.88
Sc	6.67	16.08	9.23	7.14	11.90	13.40	13.00	2.69	2.53	2.39	2.69
Cu	25.79	18.84	19.48	13.34	34.10	51.80	26.30	24.20	20.10	7.05	7.75
Pb	20.76	27.25	30.36	30.80	39.70	41.80	20.40	25.70	24.20	25.40	33.00
Zn	56.39	83.75	86.93	70.96	103.00	130.00	101.00	37.80	39.20	64.90	63.50
W	0.67	1.02	0.92	0.92	3.76	3.87	2.15	3.20	2.46	0.75	1.28
Sn	3.15	3.13	6.10	5.71	5.43	6.07	4.98	4.07	5.28	6.17	3.14

(*Continued*)

https://doi.org/10.1017/S0016756821000479 Published online by Cambridge University Press

Table 4. (*Continued*)

Rock type	Granodiorite							Porphyritic granite			
Sample No.	EGX-1a	EGX-1b	EGD-1a	EGD-1b	XSH-5a	XSH-5b	XSH-5c	EGX-2a	EGX-2b	EGX-3a	EGX-3b
Bi	0.18	0.40	0.18	0.15	0.62	0.46	0.17	1.41	0.37	0.14	0.25
Mo	0.46	3.12	3.08	2.33	1.97	1.55	0.81	14.50	9.95	8.45	8.26
La	52.38	46.33	47.08	39.22	44.80	62.10	73.00	64.60	54.90	21.90	45.70
Ce	105.21	93.23	94.79	77.20	75.10	100.00	107.00	99.80	88.40	56.20	59.70
Pr	12.77	11.54	11.72	9.27	10.70	15.00	16.20	12.90	10.30	5.08	8.83
Nd	46.44	42.89	43.52	33.79	45.90	57.20	65.50	44.50	37.00	18.50	30.50
Sm	7.73	7.11	7.27	5.44	8.73	10.60	11.30	7.47	5.98	4.10	5.29
Eu	1.25	1.21	1.29	1.15	1.18	1.23	1.70	0.58	0.43	0.36	0.43
Gd	6.97	6.52	6.55	5.03	7.28	8.85	10.00	6.32	5.28	3.48	4.67
Tb	0.99	0.94	0.94	0.80	1.40	1.65	1.74	1.09	0.85	0.64	0.74
Dy	5.07	5.25	5.00	4.63	7.17	8.11	8.90	5.60	4.50	4.00	3.88
Ho	0.99	1.00	0.96	0.91	1.54	1.55	1.77	1.14	0.90	0.82	0.78
Er	2.74	2.79	2.62	2.60	4.08	4.50	5.11	3.44	2.65	2.41	2.23
Tm	0.44	0.43	0.42	0.39	0.69	0.74	0.81	0.63	0.52	0.46	0.41
Yb	2.99	3.06	2.79	2.73	4.45	5.13	6.02	4.27	3.49	2.89	2.61
Lu	0.43	0.43	0.40	0.40	0.62	0.69	0.84	0.61	0.48	0.39	0.38
Y	28.66	28.43	27.86	23.40	45.20	51.50	55.90	34.70	28.40	23.90	22.70
ΣREE	246.41	222.72	225.34	183.54	213.64	277.35	309.89	252.95	215.68	121.23	166.15
LREE	225.78	202.31	205.67	166.07	186.41	246.13	274.70	229.85	197.01	106.14	150.45
HREE	20.62	20.42	19.68	17.49	27.23	31.22	35.19	23.10	18.67	15.09	15.70
LREE/HREE	10.95	9.91	10.45	9.50	6.85	7.88	7.81	9.95	10.56	7.03	9.58
$(La/Yb)_N$	12.57	10.86	12.10	10.30	7.22	8.68	8.70	10.85	11.28	5.44	12.56
δEu	0.51	0.53	0.56	0.66	0.44	0.38	0.48	0.25	0.23	0.28	0.26
δCe	0.97	0.96	0.96	0.96	0.81	0.78	0.73	0.80	0.85	1.26	0.68

Note: LOI: Loss on ignition; A/CNK = molecular $[Al_2O_3/(CaO + Na_2O + K_2O)]$; A/NK = molecular $[Al_2O_3/(Na_2O + K_2O)]$; $\delta Eu = Eu_N/(Gd_N + Sm_N)^{1/2}$; $(La/Yb)_N = (La/0.237)/(Yb/ 0.17)$; $Mg^{\#} = 100$ molecular $Mg^{2+}/(Mg^{2+} + Fe^{2+})$.

granodiorite exhibits values less than 4, corresponding to the ratio range of weakly differentiated granite, but the porphyritic granite exhibits values mostly greater than 4 and less than 16, corresponding to the range of differentiated granite (Whalen *et al.* 1987). In Figure 12d, the granodiorite and porphyritic granite samples plot within the undifferentiated and differentiated granite areas, respectively. Combined with the differentiation index calculation, the granodiorite (DI = 60.93–71.86) in the Ergu mining area can be considered a moderately differentiated granite, while porphyritic granite (DI = 89.93–91.80) can be considered highly differentiated granite. Therefore, we believe that the granodiorite in the study area is a moderately differentiated high-K calc-alkaline I-type granite and that the porphyry granite is a highly differentiated high-K calc-alkaline I-type granite.

6.b.2. Petrogenesis

As described above, the intrusive rocks in the Ergu mining area are high-K calc-alkaline I-type granitoids. There are three possible interpretations for the generation of intermediate to felsic high-K calc-alkaline granitoids: (a) partial melting of ancient or juvenile basaltic lower crust (Hou *et al.* 2013); (b) fractional crystallization of mantle-derived basic magma or magma crystallization formed by mixing with acidic magma (Soesoo, 2000; Fowler *et al.* 2008); and (c) partial melting of a subducted oceanic slab (Martin *et al.* 2005).

According to current research, in the Ergu metallogenic system and the Lesser Xing'an–Zhangguangcai Range (LXZR), the intrusions in this period (182–186 Ma) are mainly granodiorite and monzogranite, with a small amount of contemporaneous mafic rocks (gabbro and diorite) (accounting for less than 5 %) (Yu *et al.* 2012; Han *et al.* 2019). Consequently, it is clearly impossible to explain how such a large-scale granite is derived from the fractional crystallization of basic magma. The granodiorite and porphyry granite have relatively homogeneous Hf isotopic compositions, and the hornblende composition in granodiorite is relatively homogeneous; all of them are magnesio-hornblende. Thus, the mixing of a basic magma and an acidic magma during magma ascent can be ruled out. We also excluded the possibility of magma mixing because of no associated field and petrological evidence including mafic enclaves, basic plagioclase and quenching acicular apatite.

Experimental petrology has shown that high-K calc-alkaline I-type granitoids are generally produced by the partial melting of hydrous calc-alkaline to high-K calc-alkaline, basaltic to intermediate metamorphic rocks within the crust (Patiño Douce & Harris, 1998). The samples of granodiorite and porphyritic granite

https://doi.org/10.1017/S0016756821000479 Published online by Cambridge University Press

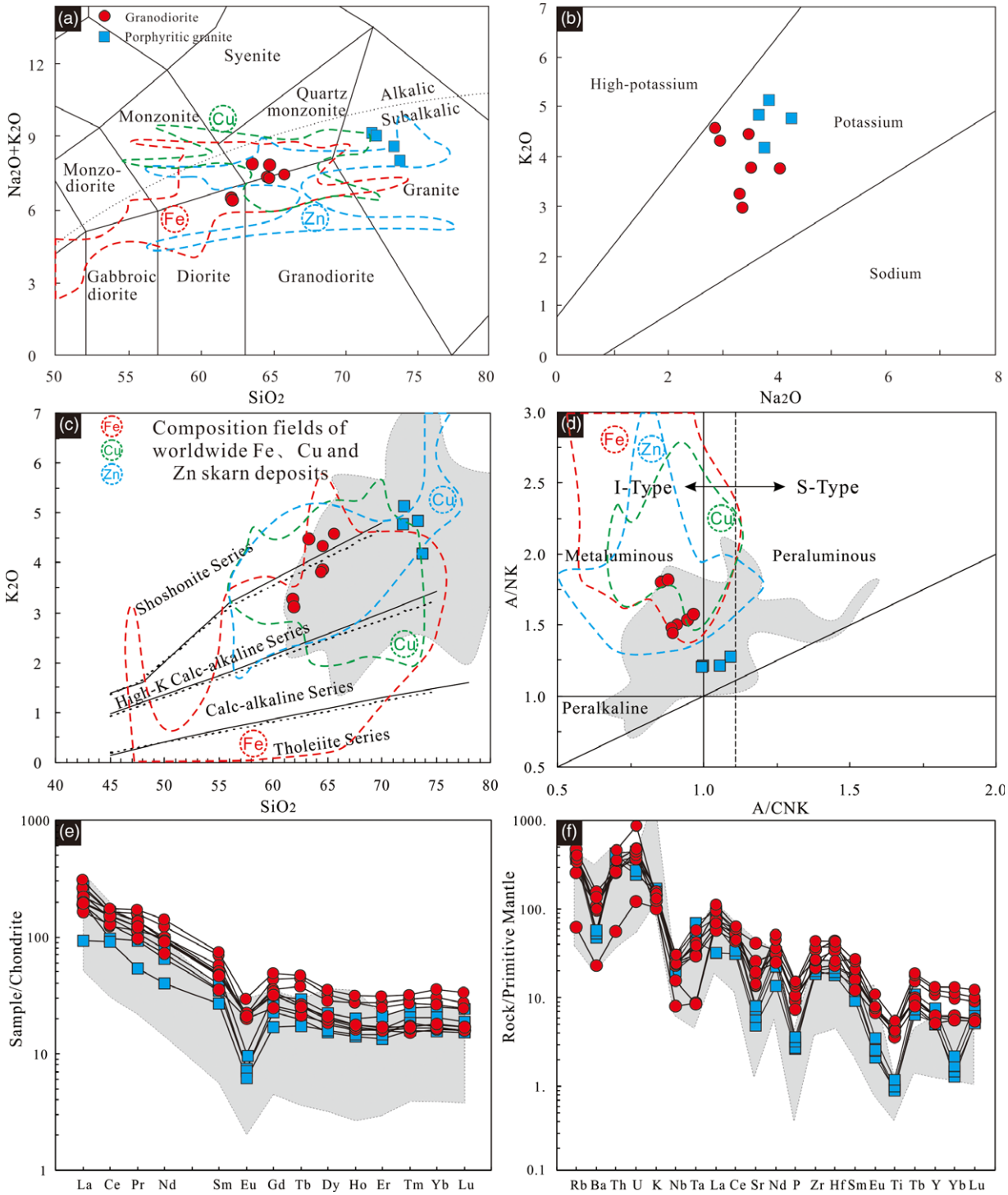

Fig. 8. (Colour online) (a) SiO_2 vs ($Na_2O + K_2O$) plot (Middlemost, 1994). (b) Na_2O vs K_2O plot (Middlemost, 1972). (c) SiO_2 vs K_2O plot (Peccerillo & Taylor, 1976). (d) A/CNK vs A/NK plot (Maniar & Piccoli, 1989). (e) Chondrite-normalized REE patterns (normalized values are from Boynton, 1984). (f) Primitive-mantle-normalized trace element patterns (normalized values are from Sun & McDonough, 1989). Average values of major element contents and the compositional fields of plutons associated with Fe, Cu, Zn and skarn deposits worldwide (Meinert, 1995; Pons *et al.* 2010) are shown for comparison (a, c, d). The shaded areas represents the Early Jurassic granite data in the Lesser Xing'an Ranfe area and are modified after Xu *et al.* (2013) and Han *et al.* (2019).

in the Ergu mining area have high SiO_2 (62.02–73.94 %) and total alkali ($Na_2O + K_2O$ = 6.50–9.11 %) contents and low $Mg^{\#}$ values (19.84–48.03), indicating that their initial magma was generated by partial melting of the lower crust or by a silica melt that experienced multistage evolution (Barbarin, 1999). In terms of trace element composition, the granodiorites and porphyritic granites show negative Nb, Ta, P and Ti anomalies, positive Rb, Th and K anomalies and enrichment of LILEs and LREEs (Fig. 8e, f), which are similar to patterns of crust-derived rocks. This similarity is supported by the ratios of certain trace elements, such as Rb/Sr = 0.05–2.59, La/Nb = 1.33–9.05 and Th/Nb = 0.82–3.17 (Saunders *et al.* 1988). As we can see from Figure 9 and

https://doi.org/10.1017/S0016756821000479 Published online by Cambridge University Press

Table 5. Hf isotopic data for zircons of intrusions from the Ergu Fe–Zn polymetallic deposit

Sample No.	Age (Ma)	$^{176}Yb/^{177}Hf$	2σ	$^{176}Lu/^{177}Hf$	2σ	$^{176}Hf/^{177}Hf$	2σ	$^{176}Hf/^{177}Hf_i$	eHf(0)	eHf(t)	T_{DM} (Ma)	T_{DM}^C(Ma)	$f_{Lu/Hf}$
Granodiorite (EGX-1)													
1	183.00	0.01915	0.000313	0.00075	0.000011	0.28274	0.000029	0.28274	−1.00	2.90	717	1039	−0.98
2	184.80	0.01142	0.000177	0.00046	0.000007	0.28269	0.000032	0.28269	−3.00	1.00	790	1163	−0.99
3	183.10	0.02432	0.000463	0.00094	0.000016	0.28277	0.000034	0.28277	−0.10	3.80	684	981	−0.97
4	184.00	0.01566	0.000205	0.00061	0.000007	0.28272	0.000029	0.28272	−1.90	2.10	748	1092	−0.98
5	183.90	0.02217	0.000368	0.00085	0.000013	0.28272	0.000028	0.28272	−1.80	2.10	752	1091	−0.97
6	184.00	0.01750	0.000452	0.00068	0.000017	0.28269	0.000034	0.28268	−3.00	0.90	795	1164	−0.98
7	183.00	0.02448	0.000387	0.00094	0.000014	0.28276	0.000030	0.28276	−0.40	3.50	697	1003	−0.97
8	183.00	0.01517	0.000102	0.00059	0.000004	0.28276	0.000034	0.28275	−0.60	3.40	696	1008	−0.98
9	183.90	0.02359	0.000607	0.00091	0.000020	0.28277	0.000028	0.28276	−0.20	3.80	686	985	−0.97
10	196.80	0.03049	0.000216	0.00117	0.000008	0.28283	0.000029	0.28283	2.00	6.20	603	841	−0.96
11	186.40	0.01443	0.000141	0.00056	0.000006	0.28271	0.000026	0.28271	−2.10	1.90	755	1102	−0.98
12	183.80	0.01463	0.000059	0.00058	0.000003	0.28273	0.000028	0.28273	−1.60	2.40	735	1071	−0.98
13	182.90	0.02459	0.000434	0.00093	0.000016	0.28279	0.000027	0.28278	0.50	4.40	660	944	−0.97
14	184.10	0.02395	0.000315	0.00090	0.000012	0.28271	0.000028	0.28271	−2.20	1.70	767	1113	−0.97
15	183.80	0.01240	0.000137	0.00050	0.000007	0.28271	0.000026	0.28271	−2.20	1.80	759	1111	−0.98
16	182.70	0.02754	0.000410	0.00103	0.000015	0.28266	0.000026	0.28265	−4.10	−0.20	846	1237	−0.97
17	183.80	0.01226	0.000131	0.00049	0.000005	0.28277	0.000029	0.28277	−0.20	3.80	678	981	−0.99
18	184.20	0.01126	0.000349	0.00046	0.000011	0.28267	0.000037	0.28267	−3.50	0.50	811	1195	−0.99
19	183.00	0.02322	0.000216	0.00089	0.000006	0.28280	0.000025	0.28280	1.10	5.10	633	902	−0.97
Granodiorite (XSH-5)													
1	182.00	0.01591	0.000250	0.00057	0.000005	0.28277	0.000025	0.28277	−0.10	3.80	679	1317	−0.98
3	182.00	0.01606	0.000060	0.00057	0.000001	0.28267	0.000020	0.28267	−3.60	0.30	816	1630	−0.98
4	184.00	0.02254	0.000240	0.00080	0.000006	0.28276	0.000022	0.28276	−0.40	3.50	694	1343	−0.98
5	182.00	0.01335	0.000040	0.00049	0.000001	0.28270	0.000019	0.28269	−2.70	1.30	778	1546	−0.99
6	202.00	0.01138	0.000050	0.00041	0.000002	0.28268	0.000021	0.28268	−3.30	1.10	799	1573	−0.99
7	178.00	0.02252	0.000340	0.00077	0.000010	0.28275	0.000016	0.28275	−0.80	3.00	710	1387	−0.98
8	181.00	0.02113	0.000140	0.00076	0.000005	0.28271	0.000019	0.28271	−2.20	1.60	765	1510	−0.98
9	183.00	0.01644	0.000260	0.00060	0.000008	0.28271	0.000019	0.28270	−2.30	1.60	766	1514	−0.98
10	183.00	0.02008	0.000350	0.00071	0.000012	0.28270	0.000018	0.28270	−2.40	1.50	772	1523	−0.98
12	183.00	0.01336	0.000040	0.00048	0.000000	0.28268	0.000020	0.28267	−3.40	0.50	806	1612	−0.99
13	183.00	0.02292	0.000220	0.00083	0.000010	0.28270	0.000021	0.28270	−2.40	1.50	774	1524	−0.97
14	180.00	0.02686	0.000560	0.00095	0.000024	0.28268	0.000019	0.28268	−3.30	0.50	812	1610	−0.97
Porphyritic granite (EGX-2)													
1	184.00	0.02660	0.000160	0.00098	0.000007	0.28283	0.000047	0.28282	1.94	5.86	602	850	−0.97
4	182.00	0.02616	0.000190	0.00099	0.000003	0.28274	0.000023	0.28274	−1.18	2.70	727	1050	−0.97
5	181.00	0.03588	0.000230	0.00143	0.000007	0.28275	0.000021	0.28275	−0.73	3.08	717	1025	−0.96
6	187.00	0.02503	0.000140	0.00098	0.000003	0.28270	0.000020	0.28270	−2.52	1.46	781	1132	−0.97
7	181.00	0.02787	0.000370	0.00105	0.000011	0.28273	0.000021	0.28272	−1.60	2.25	745	1077	−0.97
12	200.00	0.03701	0.000300	0.00141	0.000014	0.28276	0.000026	0.28275	−0.60	3.61	712	1006	−0.96
13	182.00	0.03099	0.000110	0.00115	0.000006	0.28272	0.000021	0.28272	−1.74	2.12	753	1087	−0.97
14	185.00	0.02411	0.000230	0.00091	0.000007	0.28272	0.000018	0.28272	−1.77	2.18	749	1085	−0.97
15	183.00	0.04317	0.000620	0.00157	0.000024	0.28271	0.000020	0.28270	−2.28	1.55	783	1124	−0.95
16	181.00	0.02932	0.000710	0.00111	0.000026	0.28268	0.000021	0.28268	−3.11	0.73	807	1174	−0.97

https://doi.org/10.1017/S0016756821000479 Published online by Cambridge University Press

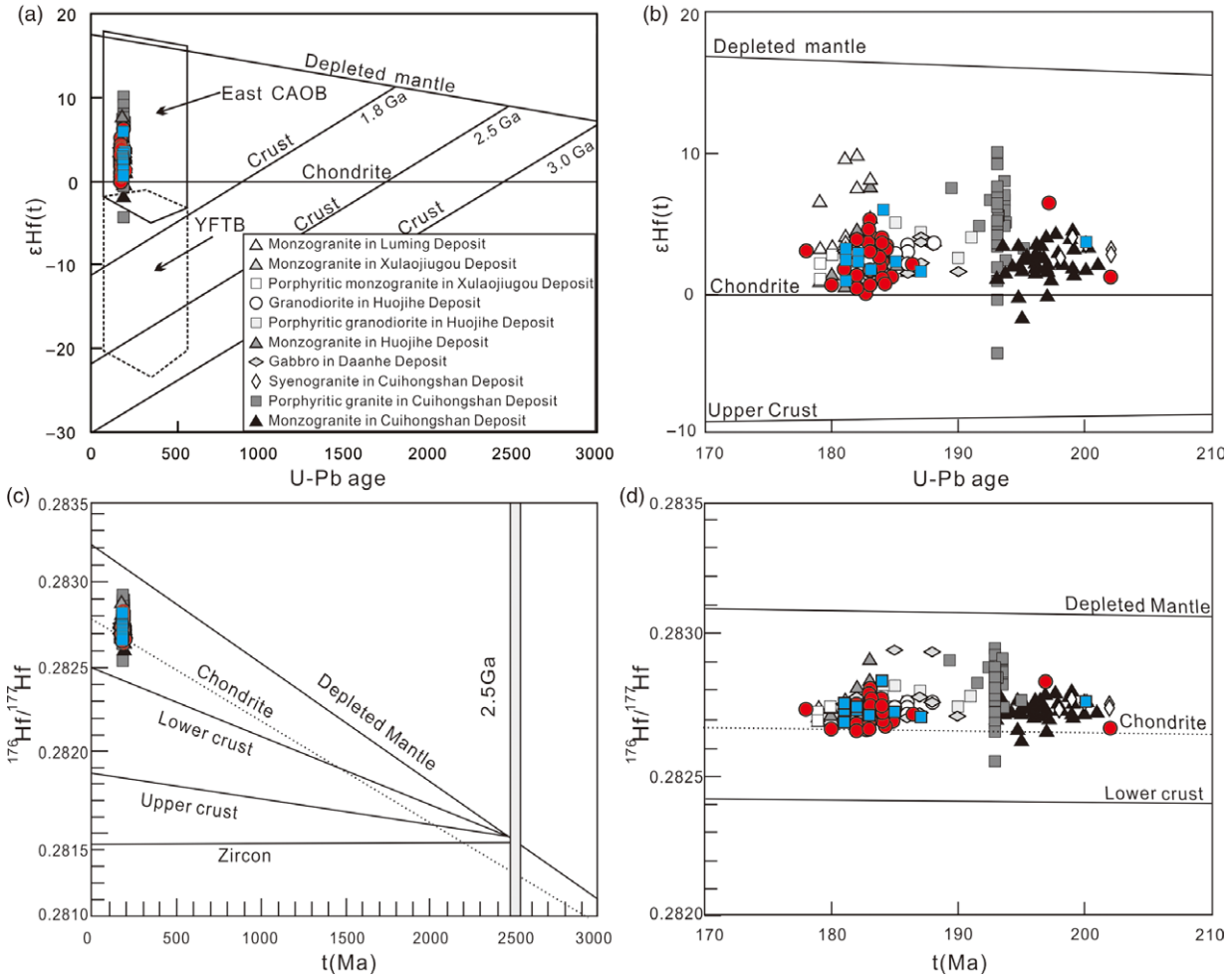

Fig. 9. (Colour online) $\epsilon_{Hf}(t)$ vs crystallization age of zircons from granodiorite and porphyritic granite of the Ergu Fe–Zn polymetallic deposit (Vervoort *et al.* 1999; Yang *et al.* 2006). Luming and Xulaojiugou deposit data are from Hu *et al.* (2014*b*), Huojihe deposit data from Hu *et al.* (2019), Da'anhe data (unpublished) from our team, and Cuihongshan deposit data from Chen *et al.* (2014) and Fei *et al.* (2018).

Table 5, zircon Hf isotopic data from the granodiorite and porphyritic granite are similar to the Hf isotopic compositions of the Phanerozoic igneous rocks in the CAOB, which suggests that the primary magmas originated from the partial melting of lower crust that formed during the Mesoproterozoic to Neoproterozoic (Han *et al.* 2019). The granodiorite closely related to the mineralization of the Ergu deposit features moderate initial $^{87}Sr/^{86}Sr$ values (0.70599 to 0.70897), weak negative $\epsilon Nd(t)$ anomalies (−1.7 to −1.4) and relatively young model ages ($T_{DM1,\ Nd}$ =919–966 Ma; $T_{DM1,\ Nd}$ = 1080–1102 Ma), which are similar to those of typical skarn–porphyry deposits in the Lesser Xing'an Range (($^{87}Sr/^{86}Sr)_i$ = 0.70071–0.70962, $\epsilon Nd(t)$ = −4.9 to +0.8, and $T_{DM2,\ Nd}$ = 812–1615 Ma; Fig. 10a, b). Moreover, in the plot of $\epsilon_{Hf}(t)$ vs $\epsilon Nd(t)$ (Fig. 10c), all the analysis points plot within the area of oceanic island basalt and lower crust, signifying that the granodiorite was probably formed by partial melting of lower crust. These results are also supported by the Pb isotopic compositions: in the plot of $^{207}Pb/^{204}Pb$ vs $^{206}Pb/^{204}Pb$ (Fig. 10d), all samples plot within the lower crust region. It is worth noting that the Sr–Nd isotope and Hf isotope data of the Ergu deposit display weak decoupling, which is similar to that of Early Jurassic intrusive rocks in the Lesser Xing'an Range area (Fig. 10). Wu *et al.* (2000) pointed out that there is a kind of granite in NE China that was emplaced within the Precambrian basement and shows negative $\epsilon Nd(t)$ values (0 to −8) and high initial $^{87}Sr/^{86}Sr$ ratios. Wang *et al.* (2014) discovered the remnant ancient basement material within the Songnen–Zhangguangcai Range Massif. In addition, Fei *et al.* (2018) believed that in the Early Jurassic, there was a metallogenic event in the Lesser Xing'an Range area, which related to Early Jurassic granite that originated from mixed sources including juvenile and Precambrian crustal materials. Therefore, we think that the intrusive rocks in the Ergu mining area were possibly generated by partial melting of crustal materials from mixed sources containing varying degrees of juvenile and Precambrian crustal materials.

Compared with granodiorite, the porphyry granite lacks Sr–Nd–Pb isotopic data, but the silicon content of porphyritic granite is obviously higher, the contents of Ba, Sr, Nb, P and Ti are obviously lower and the Eu anomaly is more obvious, which indicates that the degree of evolution of the latter is higher. Combined with the same crystallization age and similar Hf isotopic characteristics, it is very likely that the porphyry granite and granodiorite formed by comagmatic evolution controlled by different degrees of fractional crystallization. Furthermore, Han *et al.* (2019) described many intermediate-acid intrusions with genetic relationships in the LXZR, and these intrusions were controlled by fractional crystallization and successively emplaced at different stages during magma evolution. Therefore, it is reasonable to

https://doi.org/10.1017/S0016756821000479 Published online by Cambridge University Press

Table 6. Sr–Nd–Pb isotopic data for granodiorites from the Ergu Fe–Zn polymetallic deposit

Sample no.	T (Ma)	Rb (ppm)	Sr (ppm)	$^{87}Rb/^{86}Sr$	$^{87}Sr/^{86}Sr$	$(^{87}Sr/^{86}Sr)_i$	Sm (ppm)	Nd (ppm)	$^{147}Sm/^{144}Nd$	$^{143}Nd/^{144}Nd$	$(^{143}Nd/^{144}Nd)_i$	$\epsilon Nd(t)$
EGX-1a	183.8	302.3	375.5	2.3302	0.712081	0.70599	7.3	43.5	0.1009	0.512435	0.51231	−1.7
EGX-1b	183.8	249.4	410.2	1.7595	0.710711	0.70611	5.4	33.8	0.0973	0.512438	0.51232	−1.6
EGD-1a	183.8	40	866.1	0.1337	0.709317	0.70897	7.7	46.4	0.1007	0.512453	0.51233	−1.4
EGD-1b	183.8	164.7	541.7	0.8798	0.709288	0.70699	7.1	42.9	0.1002	0.51245	0.51233	−1.4
Sample No.	T_{DM1-Nd} (Ma)	T_{DM2-Nd} (Ma)	$f_{Sm/Nd}$	$^{206}Pb/^{204}Pb$	2σ	$^{207}Pb/^{204}Pb$	2σ	$^{208}Pb/^{204}Pb$	2σ	$(^{206}Pb/^{204}Pb)_t$	$(^{207}Pb/^{204}Pb)_t$	$(^{208}Pb/^{204}Pb)_t$
EGX-1a	966	1108	−0.49	18.9903	0.001	15.6155	0.0009	38.6053	0.0025	18.7603	15.604	38.4679
EGX-1b	958	1102	−0.49	18.9895	0.0009	15.6168	0.001	38.6114	0.0029	18.3944	15.5872	38.1262
EGD-1a	944	1080	−0.49	18.9571	0.0009	15.6162	0.0008	38.6933	0.0024	18.4774	15.5923	38.2145
EGD-1b	919	1078	−0.51	19.059	0.001	15.6111	0.0009	38.6796	0.0026	18.4839	15.5825	38.2307

conclude that the granodiorite magma in the Ergu mining area differentiated and evolved into the porphyry granite. Notable depletion of Eu concentrations (Fig. 8e) is considered to be associated with fractionation of plagioclase or K-feldspar (Hanson, 1978). The Rb/Sr ratios of the Ergu intrusion samples decrease with increasing Sr concentration (Fig. 13a), which may be closely related to K-feldspar differentiation or to the crystallization differentiation of plagioclase and biotite (Hanson, 1978). Biotite fractionation will induce a negative correlation between Sc/Yb and SiO_2/Al_2O_3 (Liao *et al.* 2019); the negative correlation between Sc/Yb and SiO_2/Al_2O_3 in these granites indicates that biotite is a major fractionation mineral there (Fig. 13b). Hornblende fractionation will induce a negative correlation between Dy/Sm and Zr/Sm (Sisson, 1994). There is no obvious linear relationship between these two parameters in these granodiorite and porphyry granite samples (Fig. 13c), excluding hornblende as a major fractionation phase. The depletion of HFSEs (such as Nb, Ta, Ti, Zr) and P in the Ergu
intrusive rocks indicates that Ti-bearing minerals (such as ilmenite and sphene) and apatite are crystallized during magmatic differentiation, which is consistent with the result obtained in the diagram of La vs $(La/Yb)_N$ (Fig. 13d).

Therefore, the porphyry granite and granodiorite in the Ergu mining area shared the same initial magma originating from the partial melting of crustal materials from mixed sources containing varying degrees of juvenile and Precambrian crustal materials. The porphyritic granite was probably derived from the fractional crystallization of granodiorite magma, with a subsequently extensive fractional crystallization of plagioclase, K-feldspar, biotite, apatite, Ti-bearing phases, ilmenite and sphene before the final emplacement.

6.c. Tectonic setting

The Lesser Xing'an Range, located in the eastern segment of the CAOB, underwent the evolution and final closure of the Palaeo-Asian Ocean and the amalgamation of multiple microcontinental massifs in the Palaeozoic, during which it was characterized by a large island arc system and continental margin accretion (Ren *et al.* 1999). The available data show that during the Late Permian to Early Triassic, with the final closure of the Palaeo-Asian Ocean, the North China Craton collided with the Songnen block along the Xilamulun–Changchun–Yanji line in NE China (Xiao *et al.* 2003; Sun *et al.* 2004; Wu *et al.* 2007). In the Mesozoic–Cenozoic, the study area became part of the evolution of the Circum-Pacific and Mongol–Okhotsk Ocean tectonic systems (Tomurtogoo *et al.* 2005; Sun *et al.* 2013).

For the whole of NE China, Shu *et al.* (2016) indicated that magmatic–hydrothermal deposit (porphyry, skarn and epithermal deposits) formation had a younging trend towards the northwest from 200 to 140 Ma and this trend is consistent with the time–space trends of intrusive and extrusive igneous rocks. It was interpreted that the early Yanshanian period reflected advancing Palaeo-Pacific subduction. In addition, the Early Jurassic ophiolitic melange has been recognized along the Asian continental margin (Zhou *et al.* 2009) and geophysical data have identified a residual of the previous subducted slab at a depth of 660 km beneath eastern China (Van der Voo *et al.* 1999), suggesting that the Mesozoic magmatism in the Lesser Xing'an Range is related to subduction of the Palaeo-Pacific Plate. Han *et al.* (2019) summarized the geochemical characteristics of the Early–Middle Jurassic intrusive rocks in the Lesser Xing'an

https://doi.org/10.1017/S0016756821000479 Published online by Cambridge University Press

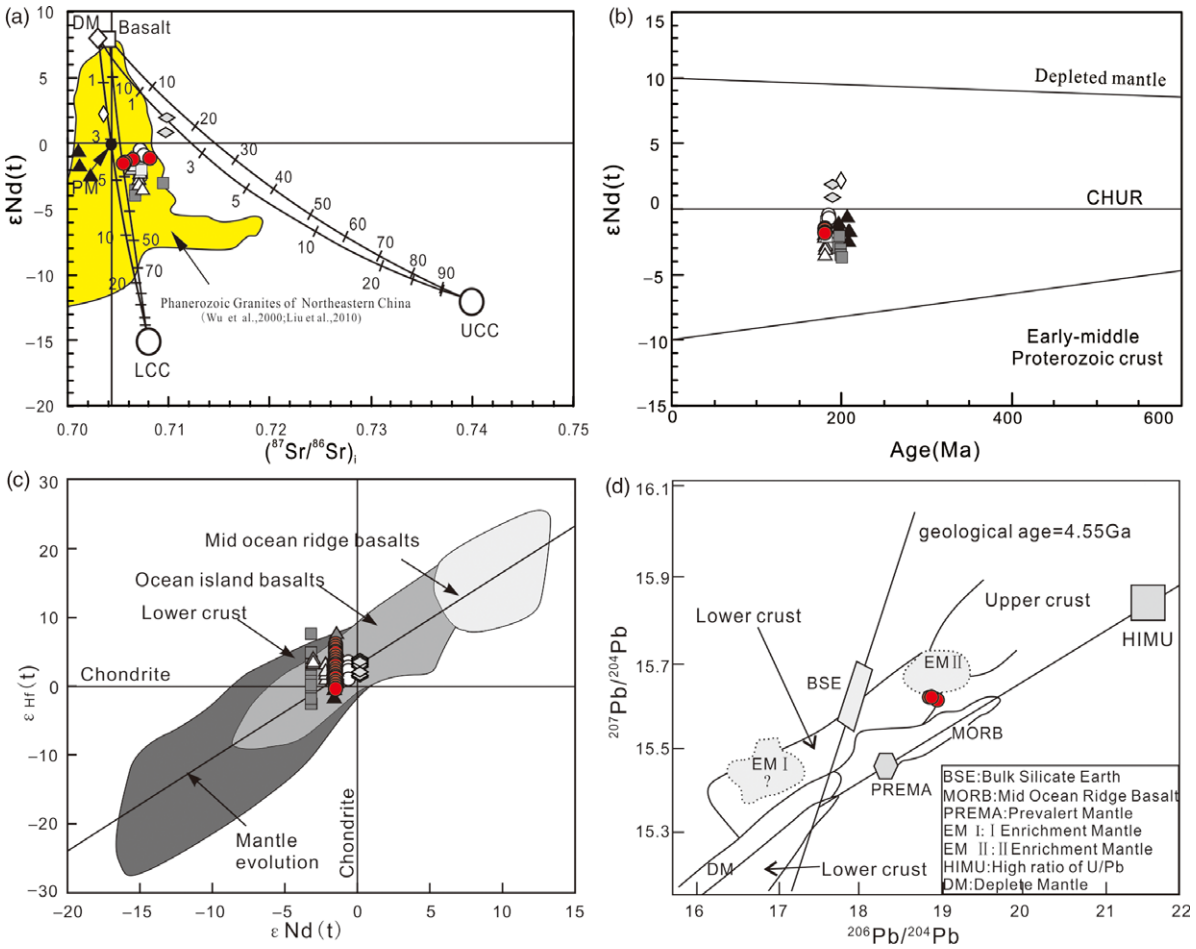

Fig. 10. (Colour online) Sr–Nd–Pb–Hf discrimination diagrams of the Early–Middle Jurassic granitoids in the Lesser Xing'an Range skarn–porphyry deposits: (a) ϵNd(t) vs ($^{87}Sr/^{86}Sr)_i$ diagram (Jahn *et al.* 2004); (b) ϵNd(t) vs crystallization age of zircons diagram (Wu *et al.* 2000); (c) plot of ϵHf(t) vs ϵNd(t) (Vervoort & Blichert-Toft 1999); (d) $^{208}Pb/^{204}Pb$ vs $^{206}Pb/^{204}Pb$ diagram (after Zartman & Doe, 1981). Luming and Xulaojiugou deposit data are from Hu *et al.* (2014*b*), Huojihe deposit data from Hu *et al.* (2019), Da'anhe data (unpublished) from our team, and Cuihongshan deposit data from Chen *et al.* (2014) and Fei *et al.* (2018).

Range, suggesting that they were formed in an active continental margin environment related to the subduction of the Palaeo-Pacific Plate. The Ergu intrusive rocks and the Early–Middle Jurassic intrusive rocks in the Lesser Xing'an Range belong to the high-K calc alkaline series (Fig. 8c), and are characterized by enrichment of LILEs and depletion of HFSEs (Fig. 8e, f), indicating that they were formed in an active continental margin environment related to subduction. Moreover, this view is supported by the tectonic discrimination diagram, in which the granitoids in the Lesser Xing'an Range fall within the volcanic arc category or active continental margin category (Fig. 14). Consequently, we consider that the Early–Middle Jurassic (201–163 Ma) magmatic events in the Lesser Xing'an Range took place in an active continental margin setting related to the subduction of the Palaeo-Pacific Plate beneath the Eurasian continent.

Therefore, we infer that the diagenesis and mineralization of the Ergu Fe–Zn polymetallic deposit took place in an active continental margin environment related to the subduction of the Palaeo-Pacific Plate beneath Eurasia.

6.d. Magmatism constraints on ore formation

For a long time, the genesis of skarn deposits has been studied in terms of the acidity and alkalinity of the magma, the wall rock properties, the emplacement depth and the oxygen fugacity. A classic concept is that the process of emplacement of hypabyssal rock or porphyry into carbonate strata is metasomatically associated. Therefore, the formation of such deposits has at least two basic conditions, namely, a hypabyssal intrusion and carbonate strata. Previous studies have shown that the intrusive rock phase is related to the precipitation of metallic elements, and the emplacement depth and oxygen fugacity define the size of the deposit (Meinert *et al.* 2005; Jiang *et al.* 2018). The study of carbonate strata closely related to mineralization in this area shows that in the Qianshan Formation, only the contents of W, Mo and Pb are relatively equal to or slightly higher than those in the crust, while the other ore-forming elements are obviously depleted (Ren, 2017). Therefore, the strata did not have the ability to provide ore-forming materials to the economic ore bodies, and the main ore-forming materials may have been provided by the associated magmatism. What are the constraints and contributions of magmatism to mineralization? The discussion is as follows.

6.d.1. Composition of the magma

Meinert (1995) systematically compiled major and trace element data for plutons related to skarn deposits worldwide and noted that the types of intrusive rocks have obvious metallogenic specificity for skarn deposits. As noted above, the granodiorites belong to the high-K calc-alkaline series, have Rb/Sr ratios of

https://doi.org/10.1017/S0016756821000479 Published online by Cambridge University Press

Table 7. Geochronological data for the Early–Middle Jurassic porphyry and skarn deposits from the Lesser Xing'an Range

Order	Deposit	Type	Main economic elements	Dating samples	Dating methods	Age (Ma)	Reference
1	Cuihongshan	Skarn	Fe–W–Mo–Zn– Pb–Cu	Molybdenite	Re–Os	203.2 ± 1.4	Zhang *et al.* 2018
2	Xiaoxilin	Skarn	Pb–Zn	Granodiorite	Zircon U–Pb	197 ± 1	Han, 2011
3	Daxilin	Skarn	Fe	Monzogranite	Zircon U–Pb	186.8 ± 1.3	Tan, 2013
4	Baishilazi	Skarn	W	Quartz diorite	Zircon U–Pb	198.3 ± 0.8	Zhao, 2014
5	Xibeihe	Skarn	Fe–Pb–Zn	Granodiorite	Zircon U–Pb	195.2 ± 1.5	Chen, 2011
6	Dananhe	Skarn	Au	Gabbro	Zircon U–Pb	203.4 ± 2.5	Yang, 2013
7	Huojihe	Porphyry	Mo	Molybdenite	Re–Os	182.4 – 179.2	Hu *et al.* 2019
8	Luming	Porphyry	Mo	Molybdenite	Re–Os	177.9 ± 2.6	Hu *et al.* 2014*b*
9	Xulaojiugou	Skarn	Pb–Zn	Monzogranite	Zircon U–Pb	181.2 ± 1.1	Hu *et al.* 2014*b*
				Porphyritic monzogranite	Zircon U–Pb	179.9 ± 1.0	
10	Ergu	Skarn	Fe–Cu–Pb–Zn–Mo	Granodiorite	Zircon U–Pb	181.9 – 183.8	This study
11	Dashihe	Porphyry	Mo	Molybdenite	Re–Os	186.7 ± 5.0	Ju *et al.* 2012
12	Wudaoling	Skarn	Mo–Fe	Quartz porphyry	Zircon U–Pb	193.6 ± 1.1	Shi *et al.* 2012
				Alkali-feldspar granite	Zircon U–Pb	193.9 ± 1.3	
13	Cuiling	Porphyry	Mo	Monzogranite porphyry	Zircon U–Pb	178 ± 0.7	Yang *et al.* 2012
14	Fuanbao	Porphyry	Mo	Molybdenite	Re–Os	170 ± 1	Zhang, 2013
15	Jidetun	Porphyry	Mo	Molybdenite	Re–Os	168 ± 2.5	Zhang, 2013
16	Liushengdian	Porphyry	Mo	Molybdenite	Re–Os	175 ± 5	Zhang, 2013
17	Qiupigou	Skarn	Cu–Fe–Mo–Pb–Zn	Syenogranite	Zircon U–Pb	184.1 ± 2.2	Wang *et al.* 2013
18	Gongpengzi	Skarn	Cu–Zn–W–Fe–Mo	Granodiorite	Zircon U–Pb	180.7 ± 2.3	Tan, 2013
19	Xinhualong	Porphyry	Mo	Molybdenite	Re–Os	171.6 ± 1.6	Zhang, 2013
20	Wulugetushan	Porphyry	Mo	Molybdenite	Re–Os	177	Mao *et al.* 2014

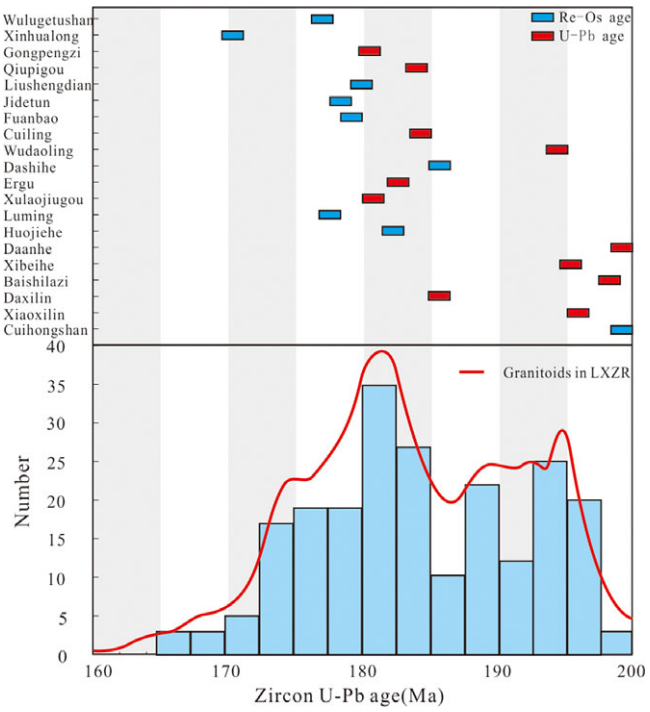

Fig. 11. (Colour online) Compilation of age data of diagenesis and skarn–porphyry deposit mineralization age in the LXZR. The LXZR granites are from Han *et al.* (2019). Sketch modified after Han *et al.* (2019). Published data are from Table 7.

0.85–0.81 < 1 and have high contents of ore elements (e.g. Cr = 23.17–44.86 ppm; V = 62.61–126.52 ppm; Pb = 20.40–41.80 ppm; and Sc = 6.67–16.08 ppm), suggesting that the granodiorites formed conditions favourable to the formation of skarn-type iron polymetallic deposits (Meinert *et al.* 2005). In addition, Figures 8a, c, d and 15 show that the granodiorites are similar to the igneous rocks associated with typical skarn-type Fe, Cu and Zn deposits worldwide (Meinert, 1995). In conclusion, it is appropriate to infer that the granodiorite is suitable for the determination of metallogenic magma in skarn-type Fe–Zn polymetallic deposits.

6.d.2. Emplacement depth of the magma

Geological and petrographic studies have revealed that the granodiorites related to mineralization in the Ergu mining area are massive and medium-grained, indicating that the magma was emplaced at a relatively large depth (>3 km) as a medium-grained plutonic intrusive rock, which is consistent with the emplacement depth calculated by amphibole composition (2.90–3.49 km; average value 3.13 km). This conception is contrary to the traditional interpretation of skarn and porphyry mineralization, and large-sized skarn iron polymetallic deposits are not easily formed under such conditions (Sillitoe, 2010). We found that the size of the deposit is affected by the depth of magma emplacement, in other words, the shallower the emplacement of the ore-related intrusive rocks, the larger the size of the deposit. Such deposits include the Daxilin skarn Fe deposit (small-sized deposit related to fine-grained biotite monzogranites, which represent deep facies

https://doi.org/10.1017/S0016756821000479 Published online by Cambridge University Press

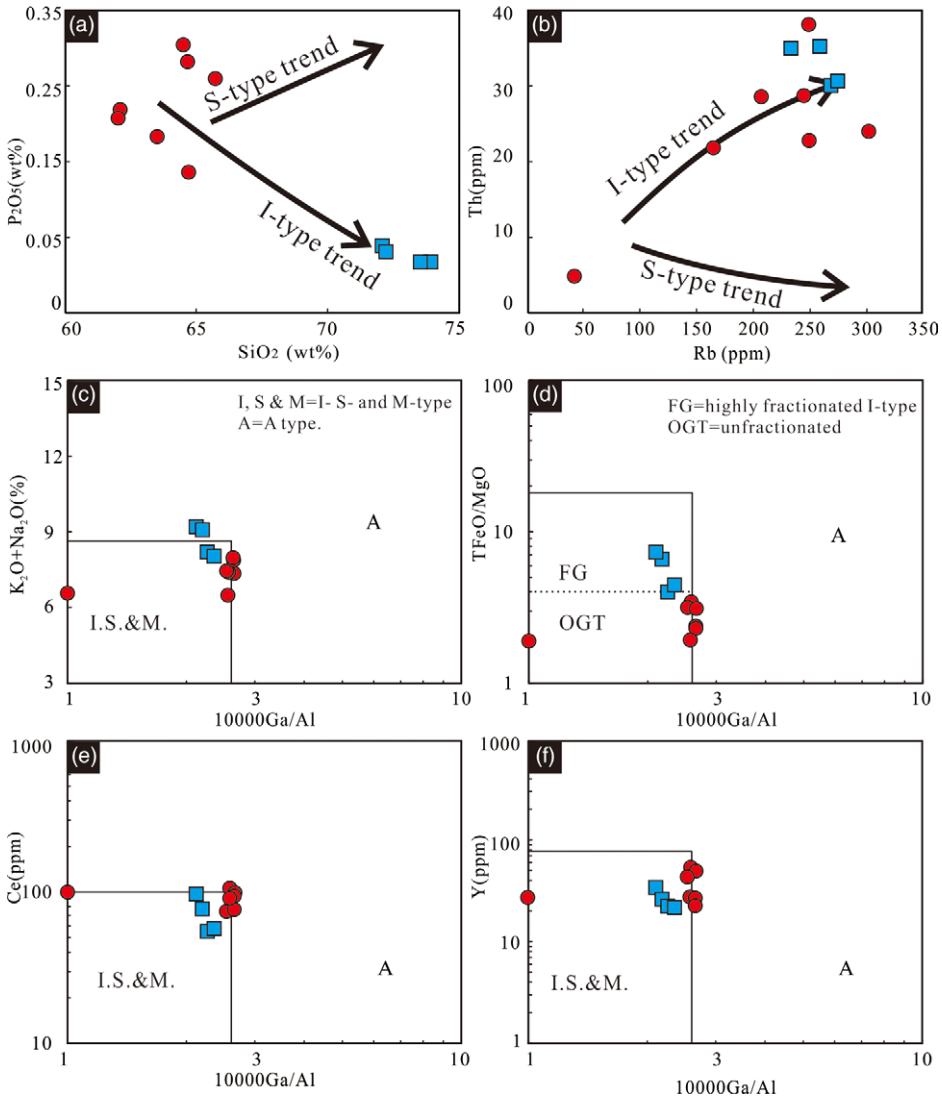

Fig. 12. (Colour online) (a) SiO_2 vs P_2O_5 plot. Trends of the I- and S-type granites are from Chappell & White (1992). (b) Th vs Rb plot. Trends of the I- and S-type granites are from Chappell & White, 1992. (c)–(f) Discrimination diagrams of $K_2O + Na_2O$ vs 10 000 Ga/Al, TFeO/MgO vs 10 000 Ga/Al, Ce vs 10 000 Ga/Al, Y vs 10 000 Ga/Al (Whalen *et al.* 1987).

(>3 km; Li *et al.* 2015), the Ergu skarn Fe–Zn deposit (medium-sized deposit with 17.31 Mt Fe at 35 % associated with moderately deep facies (3.13 km); this study) and the Cuihongshan skarn Fe-polymetallic deposit (large deposit with 68.35 Mt Fe at 48 % associated with porphyritic granite that represents shallow facies (<3 km; Fei *et al.* 2018). This feature is similar to that of skarn-type iron polymetallic deposits in the Qiman Tage area, Qinghai Province, Eastern Kunlun Orogen, China (Zhao *et al.* 2013; Yao *et al.* 2017). Previous studies have shown that the emplacement depth of the middle magma chamber will affect the size of the deposit by affecting the volume of magma and magma exsolution fluid (Chiaradia & Caricchi, 2017; Chiaradia, 2020). On the other hand, the intrusion of ore-related rocks in a deeper position is not conducive to the release of CO_2 generated by contact metasomatism between the intrusions and carbonate strata, thus affecting the continuous occurrence of mineralization (Ren, 2017). Therefore, the metallogenic size of the Ergu Fe–Zn polymetallic metallogenic system is affected by the emplacement depth of the intrusion.

Although the emplacement depth limited the size of the Ergu deposit, the latest research shows that the water-rich and oxidized parent magma can extract more ore-forming materials from the source area, reduce subsolidus of silicate minerals and prolong the magmatic differentiation time, which is conducive to the formation of metal-rich magmatic hydrothermal fluid (Richards, 2011; Sun *et al.* 2015; Chelle-Michou *et al.* 2017). Therefore, was the formation of the Ergu deposit related to a water-rich and high oxygen fugacity magma?

6.d.3. Water content and oxygen fugacity of the magma

As described above, the Ergu deposit formed in a magmatic arc environment on the active continental margin; in this environment, magma contains a certain amount of water and other components derived from the subducting plates (Hou *et al.* 2020). Recent studies have shown that the appearance of amphibole in granite indicates that the melt crystallized under relatively rich-water conditions (meltwater contents of more than 4 %) (Zhao *et al.* 2017). The H_2O content of the melt that formed the granodiorite is estimated by the amphibole compositions to be 5.23–6.17 wt %, with an estimated error of 0.4 wt %, which is also indicative of a water-rich hydrous magma. High water content in magma can also promote the enrichment of iron, and magma with high water content is more likely to dissolve ore-bearing fluid

https://doi.org/10.1017/S0016756821000479 Published online by Cambridge University Press

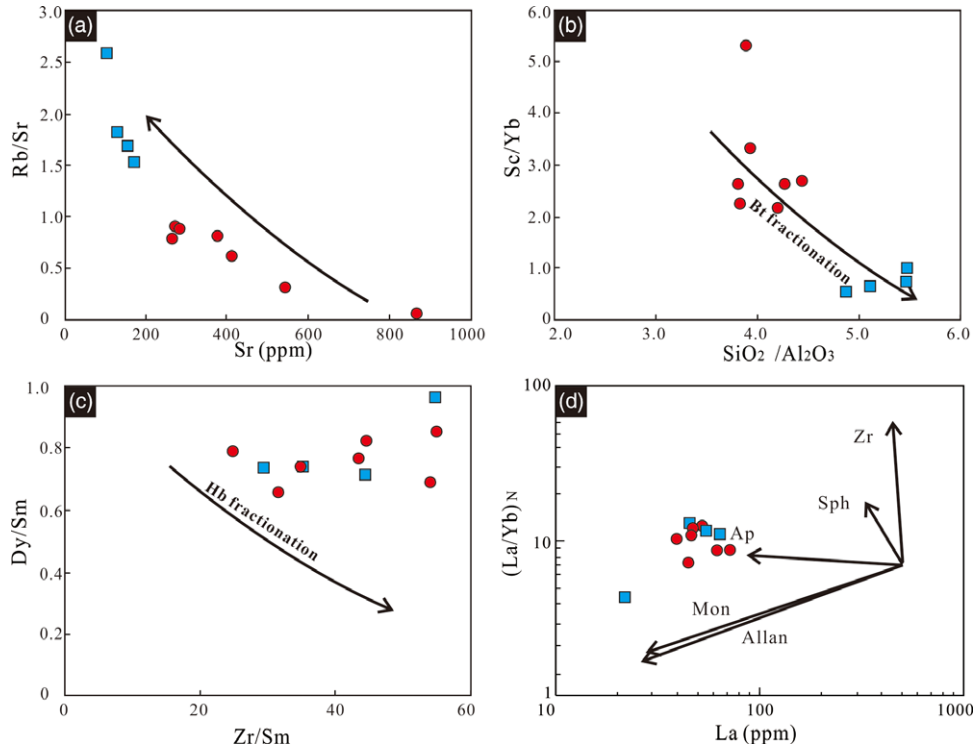

Fig. 13. (Colour online) (a) Rb/Sr vs Sr plot. (b) Sc/Yb vs SiO_2/Al_2O_3, (c) Dy/Sm vs Zr/Sm and (d) $(La/Yb)_N$ vs La (after Liao *et al*. 2019) diagrams. Pl = plagioclase; Kfs = K-feldspar; Bt = biotite; Hbl = hornblende; Zr = zircon; Sph = titanite; Ap = apatite; Mon = monazite; Allan = allanite.

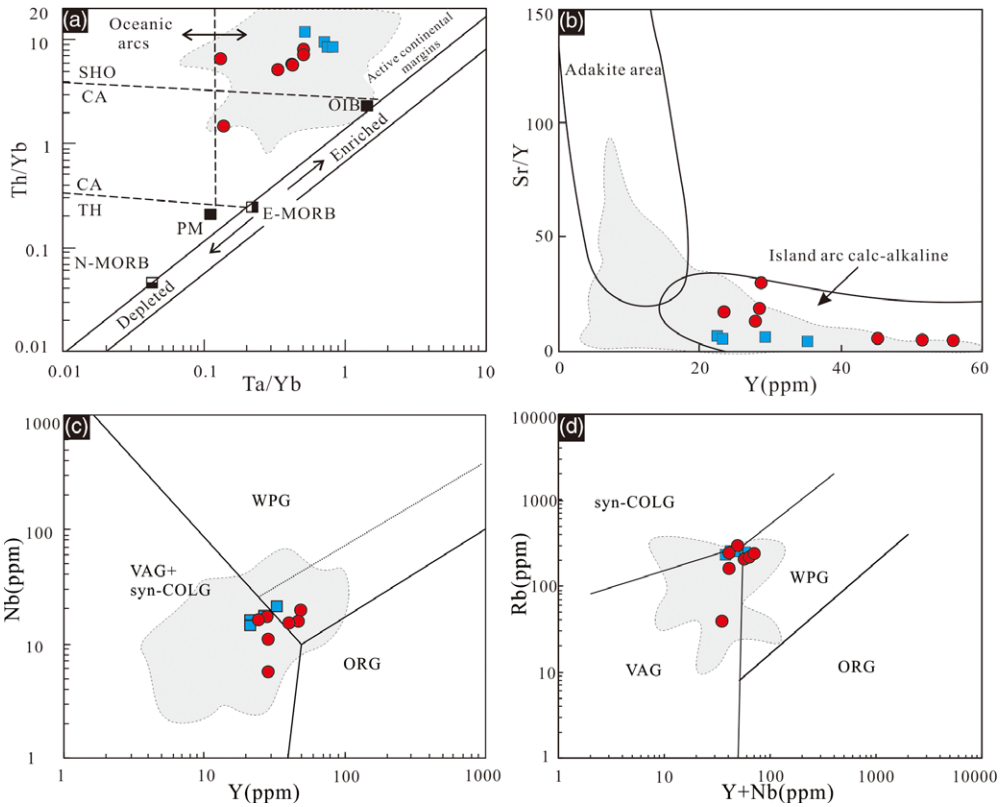

Fig. 14. (Colour online) (a) Th/Yb vs Ta/Yb plot (Pearce & Norry, 1983). (b) Sr/Y vs Y plot (Defant & Drummond, 1990). (c) Nb vs Y plot (Pearce *et al*. 1984). (d) Rb vs Y + Nb plot (Pearce *et al*. 1984). The shaded areas represents the Early Jurassic granite data in the Lesser Xing'an Ranfe area and are modified after Xu *et al*. (2013) and Han *et al*. (2019).

https://doi.org/10.1017/S0016756821000479 Published online by Cambridge University Press

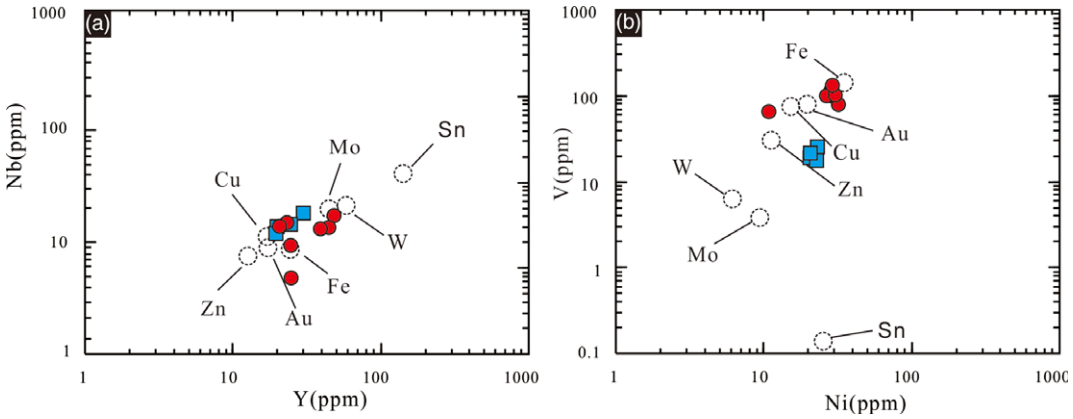

Fig. 15. (Colour online) (a) Nb vs Y and (b) V vs Ni correlation diagrams for intrusions associated with Fe and Cu mineralization at Ergu deposit. Open circles indicate the average compositions of plutons associated with skarn deposit types worldwide (Meinert 1995).

(Cline, 1995; Robb, 2005) and volatiles under low pressure. In the early stage, the dissolution of aqueous fluid can prevent the loss of metal elements, so that a large amount of iron ore can be precipitated in the later stage (Mustard *et al.* 2006). Thus, the high water content of mineralized granodioritic magmas may have played a key role in controlling the formation of the Ergu deposit.

Oxygen fugacity plays an important role in the enrichment of Fe and Cu during magma evolution (Meinert *et al.* 2005; Sillitoe, 2010; Yao *et al.* 2017). Recent studies have shown that the magma oxidation state can be determined using the trace elements in zircons (Ballard *et al.* 2002). Calculations show that the granodioritic magma of the Ergu deposit had a high oxygen fugacity ($lgfo_2$ = −15.51 to −7.33, average value = −11.70) with ΔFMQ = −1.55 to + 5.55 (average value = +1.82), which is close to the oxygen fugacity of the parent magma of the porphyry deposit (ΔFMQ = +2) (Sillitoe, 2010; Hou *et al.* 2020). Similar to the zircon calculation results, we estimated that the fO_2 of magma using amphibole had a high oxygen fugacity ($lgfo_2$ = −14.94 to −13.92, average value = −14.35) with ΔFMQ = +1.63 to + 1.97 (average value = +1.75), suggesting an oxidizing state during amphibole crystallization from shallow (3.13 km) magma chambers. The higher oxygen fugacity is also reflected in the mineral assemblages of quartz–magnetite–amphibole–biotite in the Ergu granodiorite (Li *et al.* 2016). Figure 7b shows that the Ergu granodiorite oxygen fugacity mainly plots between the fayalite–magnetite–quartz (FMQ) and magnetite–hematite (MH) buffers. Most of the points are concentrated between the Ni–NiO (NNO) buffer curve and the MH buffer line, which also confirms that the magma of the granodiorite had a high oxygen fugacity. Under the condition of high oxygen fugacity, S would have been present as sulphates (SO_4^{2-}) (Carroll & Rutherford, 1985; Richards, 2003), which can prevent the chalcophile elements (such as Fe, Cu and Mo) from being incorporated into silicate minerals (e.g. amphibole, biotite and plagioclase) as sulphide inclusions (Li *et al.* 2008). In conclusion, under high oxygen fugacity conditions, these elements can be retained in the magma and hydrothermal fluid and then enriched in the fluid phase after magma crystallization, thus promoting subsequent mineralization.

As a comparison, although the crystallization age of the porphyry granite is similar to that of the granodiorite, the porphyritic structure indicates that the porphyry granite was emplaced in the shallow crust. Compared to the granodiorite, the porphyry granite has lower oxygen fugacity ($lgfo_2$ = −20.10 to −13.57, average value is −16.07) with ΔFMQ = −4.56 to +1.78 (average value = −0.47), which might be related to the fractional crystallization of magnetite and lower Mn apatite (Sun *et al.* 2004; Zhong *et al.* 2018). In the plot of $lgfo_2$ vs *T*, the analysis points mainly plot within the area below the NNO buffer line, which also indicates that the porphyry granite magma has a lower oxygen fugacity during crystallization. This may be an important reason why the porphyry granite did not form mineralization.

In summary, we believe that the high water content, high oxygen fugacity and medium-deep emplacement of the granodiorite magma limited the Ergu deposit to being a medium-sized Fe–Zn polymetallic skarn deposit, while the water-rich, reduced and shallowly emplaced granitic magma was not conducive to mineralization.

Based on the regional tectonic evolution history, newly obtained geochemical data and geochronology data, we believe that the Ergu deposit was formed in the late Early Jurassic, which corresponded to the beginning of the subduction of the Pacific Plate beneath the Eurasian continent. In this tectonic setting, upwelling of the asthenosphere and decompression of the lithosphere caused partial melting of the lower crust and subsequent formation of the primitive basaltic magma chamber. In the process of ascent, gabbro, granodiorite and granitic magma formed successively by crystallization differentiation and were successively emplaced at different stages (Han *et al.* 2019). When the granodioritic magma was emplaced in the medium-deep position in the upper crust, widespread contact metasomatism occurred with the calcareous carbonate strata of the Qianshan Formation, forming magma fluids containing ore-forming elements such as Fe, Cu, Pb and Zn. Then, in response to reductions in temperature and pressure, crystallization of prograde skarn and retrograde skarn stages occurred. Finally, magnetite ore bodies, magnetite–sphalerite ore bodies, Cu-polymetallic ore bodies and Pb–Zn ore bodies formed in the Ergu deposit (Fig. 16).

7. Conclusions

Based on the zircon U–Pb ages, element geochemistry, zircon Hf isotopic compositions and Sr–Nd–Pb isotopic compositions of the Ergu intrusions as well as regional geological observations, we arrived at the following conclusions:

https://doi.org/10.1017/S0016756821000479 Published online by Cambridge University Press

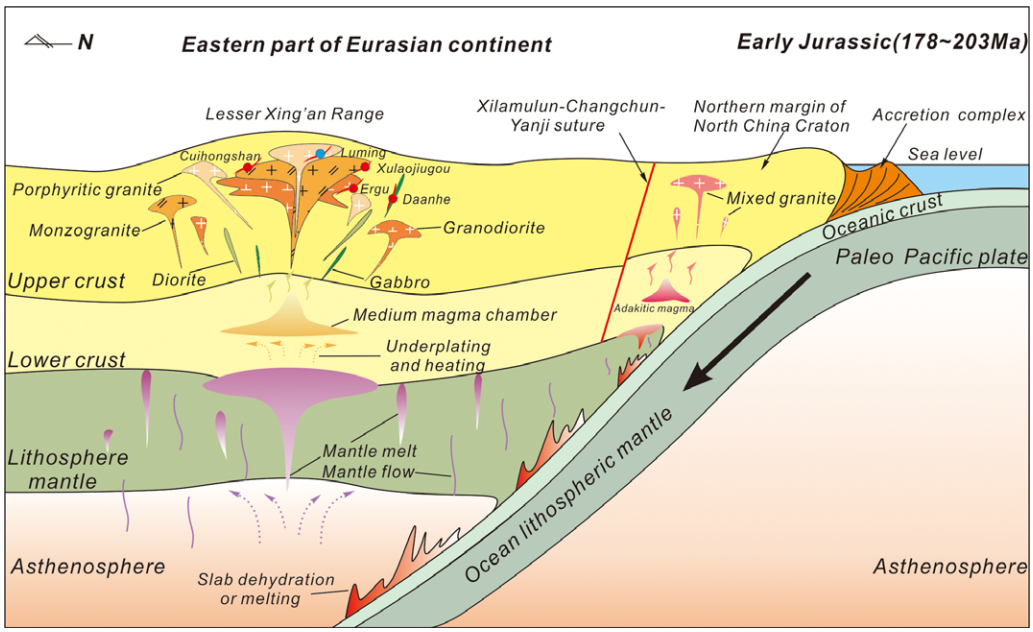

Fig. 16. (Colour online) Sketch showing the genetic model and tectonic setting for the Early Jurassic porphyry–skarn mineralization in the Lesser Xing'an Range. Modified after Han *et al.* (2019).

(1) The Ergu granodiorite and porphyry granite yield U–Pb ages of 181.9 ± 1.6 to 183.8 ± 0.65 Ma and 182.7 ± 1.4 to 182.7 ± 1.8 Ma, respectively. Combined with the ^{40}Ar–^{39}Ar age of phlogopite (181.0 ± 4.2 Ma; Ouyang & Che, 2016), these ages indicate that the magmatism and mineralization of the Ergu Fe–Zn polymetallic deposit occurred during the Early Jurassic.

(2) The geochemical and isotopic data from the Ergu intrusions imply that they were the product of comagmatic evolution with different degrees of fractional crystallization and were possibly generated by partial melting of crustal materials from mixed sources containing varying degrees of juvenile and Precambrian crustal materials. The tectonic environment was an active continental margin related to the continuous subduction of the Palaeo-Pacific Plate beneath the Eurasian continent.

(3) The high water content (>4 %), high oxygen fugacity and medium-deep emplacement of the granodioritic magma were key factors in the formation of the Ergu medium-sized Fe–Zn polymetallic skarn deposit, while the water-rich (>4 %), reduced and shallowly emplaced granitic magma was not conducive to mineralization.

Acknowledgements. This work was supported by the National Key Research and Development Program of China (Grant No. 2017YFC0601306) and the Self-determined Foundation of Key Laboratory of Mineral Resources Evaluation in Northeast Asia, Ministry of Natural Resources, Changchun, China (Grant No. DBY-ZZ-19-27), as well as the Program of the China Geological Survey (Grant No. DD20190368).

Conflicts of interest. No conflict of interest exists in the submission of the manuscript. It is approved by all the authors for publication.

References

Andersen T (2002) Correction of common lead in U-Pb analyses that do not report ^{204}Pb. *Chemical Geology* **192**, 59–79.

Ballard JR, Palin MJ and Campbell IH (2002) Relative oxidation states of magmas inferred from Ce (IV)/Ce (III) in zircon: application to porphyry copper deposits of northern Chile. *Contributions to Mineralogy and Petrology* **144**, 347–64.

Barbarin B (1999) A review of the relationships between granitoid types, their origins and their geodynamic environments. *Lithos* **46**, 605–26.

Boynton WV (1984) Geochemistry of the rare earth elements, meteorite studies. In *Rare Earth Element Geochemistry* (ed. P Henderson), pp. 63–114.. Amsterdam: Elsevier.

Carroll MR and Rutherford MJ (1985) Sulfide and sulfate saturation in hydrous silicate melts. *Journal of Geophysical Research – Atmosphere* **90**, 601–12.

Chambefort I, Dilles JH and Longo AA (2013) Amphibole geochemistry of theYanacocha volcanics, Peru: evidence for diverse sources of magmatic volatiles related to gold ores. *Journal of Petrology* **54**, 1017–46.

Chappell B and White AJR (2001) Two contrasting granite types: 25 years later. *Australian Journal of Earth Sciences* **48**, 489–99.

Chappell BW (1999) Aluminium saturation in I- and S-type granites and the characterization of fractionated haplogranites. *Lithos* **46**, 535–51.

Chappell BW and White AJR (1974) Two contrasting granite types. *Pacific Geology* **8**, 173–4.

Chappell BW and White AJR (1992) I- and S-type granites in the Lachlan Fold Belt. *Transactions of the Royal Society of Edinburgh: Earth Sciences* **83**, 1–26.

Chelle-Michou C, Rottier B, Caricchi L and Simpson G (2017) Tempo of magma degassing and the genesis of porphyry copper deposits. *Scientific Reports* **7**, 40566.

Chen J (2011) *Metallogenic setting and metallogenesis of nonferrous-precious metals in Lesser Hinggan Mountain, Heilongjiang Province*. MS thesis, Jilin University, Changchun, China (in Chinese with English abstract).

Chen L and Zhang Y (2018) In situ major-, trace-elements and Sr-Nd isotopic compositions of apatite from the Luming porphyry Mo deposit, NE China: constraints on the petrogenetic-metallogenic features. *Ore Geology Review* **94**, 93–103.

Chen X, Liu JJ, Zhang QB, Yang ZH, Yang LB and Wu J (2014) Characteristics of Hf isotopes and zircon U-Pb ages of granites in the Cuihongshan iron polymetallic deposit, Heilongjiang and their geologic implications. *Bulletin of Mineralogy, Petrology and Geochenistry* **33**, 636–44 (in Chinese with English abstract).

Chiaradia M (2020) Gold endowments of porphyry deposits controlled by precipitation efficiency. *Nature Communications* 11, 248. doi: 10.1038/s41467-019-14113-1.

Chiaradia M and Caricchi L (2017) Stochastic modelling of deep magmatic controls on porphyry copper deposit endowment. *Scientific Reports* **7**. doi: 10.1038/srep44523.

Cline JS (1995) Genesis of porphyry copper deposits: the behavior of water, chloride, and copper in crystallizing melts. In *Porphyry Copper Deposits of the American Cordillera* (eds FW Pierce and JG Bohm), pp. 69–82. Tucson: Arizona Geological Society.

Defant MJ and Drummond MS (1990) Derivation of some modern arc magmas by melting of young subducted lithosphere. *Nature* **347**, 662–5.

Fei XH, Zhang ZC, Cheng ZG, Santosh M, Jin ZL, Wen BB, Li ZX and Xu LJ (2018) Highly differentiated magmas linked with polymetallic mineralization: a case study from the Cuihongshan granitic intrusions, Lesser Xing'an Range, NE China. *Lithos* **302–303**, 158–77.

Ferry JM and Watson EB (2007) New thermodynamic models and revised calibrations for the Ti-in-zircon and Zr-in-rutile thermometers. *Contributions to Mineralogy and Petrology* **154**, 429–37.

Fowler MB, Kocks H, Darbyshire DPF and Greenwood PB (2008) Petrogenesis of high Ba-Sr plutons from the northern highlands Terrane of the British Caledonian Province. *Lithos* **105**, 129–48.

Gao FH, Wang F, Xu WL and Yang Y (2013) Age of the " Paleoproterozoic" Dongfengshan group in the lesser Xing'an range, NE China, and its tectonic implications: constraints from zircon U-Pb geochronology. *Journal of Jilin University (Earth Science Edition)* **43**, 440e456 (in Chinese with English abstract).

Geng JZ, Qiu KF, Gou ZY and Yu HC (2017) Tectonic regime switchover of Triassic Western Qinling Orogen: constraints from LA-ICP-MS zircon U-Pb geochronology and Lu-Hf isotope of Dangchuan intrusive complex in Gansu, China. *Chemie der Erde* **77**, 637–51.

Hamilton PJ, O'Nions RK, Bridgwater D and Nutman A (1983) Sm-Nd studies of Archaean metasediments and metavolcanics from West Greenland and their implications for the Earth's early history. *Earth and Planetary Science Letters* **62**, 263–72.

Han JL, Sun JG, Liu Y, Ren L, Wang CS, Zhang XT, He YP, Yu RD and Lu Q (2019) Jurassic granitic magmatism in the lesser Xing'an-Zhangguangcai ranges of NE China: the Dong'an example. *International Geological Review*. **61**, 2143–2163.

Han ZZ (2011) *Characteristics of temporal and spatial evolution and polymetallic mineralization of Early Mesozoic granites in southeastern XiaoXing'An Mountains*. MS thesis, China University of Geosciences, Beijing, China (in Chinese with English abstract).

Hanson GN (1978) The application of trace elements to the petrogenesis of igneous rocks of granitic composition. *Earth and Planetary Science Letters* **38**, 26–43.

Hao YJ, Ren YS, Yang Q, Duan MX, Sun Q, Fu LC and Li C (2015) Ore genesis and formation age of the Gaogangshan Mo deposit, Heilongjiang Province, NE China. *Resource Geology* **65**, 177–92.

Hedenquist JW and Lowenstern JB (1994) The role of magmas in the formation of hydrothermal ore deposits. *Nature* **370**, 519–27.

Heilongjiang Bureau of Geology and Mineral Resources (1993) *Regional Geology of Heilongjiang Province*. Beijing: Geological Publishing House (in Chinese).

Hoskin PWO and Schaltegger U (2003) The composition of zircon and igneous and metamorphic petrogenesis. *Reviews in Mineralogy and Geochemistry* **53**, 27–62.

Hou ZQ, Yang ZM, Wang R and Zheng YC (2020) Further discussion on porphyry Cu-Mo-Au deposit formation mainland China. *Earth Science Frontiers* **27**, 20–44 (in Chinese with English abstract).

Hou ZQ, Zheng YC, Yang ZM, Rui ZY, Zhao ZD, Jiang SH and Sun QZ (2013) Contribution of mantle components within juvenile lower-crust to collisional zone porphyry Cu systems in Tibet. *Mineralogica Deposita* **48**, 173–92.

Hu XL, Ding ZJ, He MC, Yao SZ, Zhu BP, Shen J and Chen B (2014a) Two epochs of magmatism and metallogeny in the Cuihongshan Fe-polymetallic deposit, Heilongjiang Province, NE China: constraints from U-Pb and Re-Os geochronology and Lu-Hf isotopes. *Journal of Geochemical Exploration* **143**, 116–26.

Hu XL, Ding ZJ, He MC, Yao SZ, Zhu BP, Shen J and Chen B (2014b) A porphyry-skarn metallogenic system in the Lesser Xing'an Range, NE China: implications from U-Pb and Re-Os geochronology and Sr-Nd-Hf isotopes of the Luming Mo and Xulaojiugou Pb-Zn deposits. *Journal of Asian Earth Sciences* **90**, 88–100.

Hu XL, Yao SZ, Zeng GP, Liu WH and Zhang ZJ (2019) Multistage magmatism resulting in large-scale mineralizaion: a case from the Huojihe porphyry Mo deposit in NE China. *Lithos* **326–327**, 397–414.

Irvine TN and Baragar WRA (1971) A guide to the chemical classifification of the common volcanic rocks. *Canadian Journal of Earth Sciences* **8**, 523–48.

Jahn BM, Capdevila R, Liu DY, Vernon A and Badarch G (2004) Sources of Phanerozoic granitoids in the transect Bayanhongor-Ulaan Baatar, Mongolia: geochemical and Nd isotopic evidence, and implications for Phanerozoic crustal growth. *Journal of Asian Earth Sciences* **23**, 629–53.

Jahn BM, Wu FY and Chen B (2000) Granitoids of the Central Asian Orogenic Belt and continental growth in the Phanerozoic. *Transactions of the Royal Society of Edinburgh* **91**, 181–93.

Jiang H, Jiang SY, Li WQ, Zhao KD and Peng NJ (2018) Highly fractionated Jurassic I-type granites and related tungsten mineralization in the Shirenzhang deposit, northern Guangdong, South China: evidence from cassiterite and zircon U-Pb ages, geochemistry and Sr-Nd-Pb-Hf isotopes. *Lithos* **312**, 186–203.

Ju N, Ren YS, Wang C, Wang H, Zhao HL and Qu WJ (2012) Ore genesis and molybdenite Re-Os dating of Dashihe molybdenum deposit in Dunhua, Jilin. *Global Geology* **31**, 68–76 (in Chinese with English abstract).

Li JF, Wang KY, Quan HY, Sun FY, Zhao LS and Zhang XB (2016) Discussion on the magmatic evolution sequence and metallogenic geodynamical setting background Hongling Pb-Zn deposit in the southern Da Xing'an Mountains. *Acta Petrologica Sinica* **32**, 1529–42 (in Chinese with English abstract).

Li JW, Zhao XF, Zhou MF, Vasconcelos P, Ma CQ, Deng XD, Souza ZS, Zhao YX and Wu G (2008) Origin of the Tongshankou porphyry-skarn Cu-Mo deposit, eastern Yangtze craton, Eastern China: geochronological, geochemical, and Sr-Nd-Hf isotopic constraints. *Mineralogical Deposita* **43**, 315–36.

Li JY 1999 Formation andevolution of the crust in the northern Changbaishan. Geological Publishing House, pp. 137.

Li SC, Han ZZ, Niu YH, Zhang YL, Wang X, Cheng ZX and Zheng T (2015) Determination of ages of metallogenic monzonitic intrusion and geological implication in the Xilin Pb-Zn-Fe ore deposit, Yichun, Heilongjiang Province granite. *Mineral Exploration* **6**, 356–63 (in Chinese with English abstract).

Li WK, Cheng YQ and Yang ZM (2019) Geo-fO_2: integrated software for analysis of magmatic oxygen fugacity. *Geochemistry, Geophysics, Geosystems* **20**, 2542–55. doi:10.1029/2019GC008273.

Li XH, Qi CS, Liu Y, Liang XR, Tu XL, Xie LW and Yang YH (2005) Petrogenesis of the neoproterozoic bimodal volcanic rocks along the western margin of the Yangtze Block: new constraints from Hf isotopes and Fe/Mn ratios: *Chinese Science Bulletin* **50**, 2481–6 (in Chinese with English abstract).

Liao XD, Sun S, Huan-Zhao Chi HZ, Jia DY, Ze-Yu Nan ZY and Wen-Na Zhou WN (2019) The Late Permian highly fractionated I-type granites from Sishijia pluton in southeastern Inner Mongolia, North China: a post-collisional magmatism record and its implication for the closure of Paleo-Asian Ocean, Lithos 328–329, 262–75.

Liu Y, Sun JG, Han JL, Ren L, Gu AL, Zhao KQ and Wang CS (2019) Origin and evolution of ore-forming fluid for the Gaosongshan gold deposit, Lesser Xing'an Range: evidence from fluid inclusions, H-O-S-Pb Isotopes. Geoscience Frontiers 10, 1961–80.

Ludwig KR (2003) *User's Manual for Isoplot 3.0: A Geochronological Toolkit for Microsoft Excel*. Berkeley, CA: Berkeley Geochronology Center, *Special Publication* No. **4**, —74 pp.

Lugmair GW and Harti K (1978) Lunar initial $^{143}Nd/^{144}Nd$: differential evolution of the lunar crust and mantle. *Earth and Planetary Science Letters* **39**, 349–57.

Maniar PD and Piccoli PM (1989) Tectonic discrimination of granitoids. *Geological Society of America Bulletin* **101**, 635–43.

Mao JW, Pirajno F, Lehmann B, Luo MC and Berzina A (2014) Distribution of porphyry deposits in the Eurasian continent and their corresponding tectonic settings. *Journal of Asian Earth Sciences* **79**, 576–84.

Martin H, Smithies RH, Rapp R, Moyen JF and Champion D (2005) An overview of adakite, tonalite-trondhjemite-granodiorite (TTG), and sanukitoid: relationships and some implications for crustal evolution. *Lithos* **79**, 1–24.

Meinert LD (1995) Compositional variation of igneous rocks associated with skarn deposits:chemical evidence for a genetic connection between petrogenesis and mineralization. *Mineralogical Association of Canada Short Course Series* **23**, 401–18.

Meinert LD, Dipple GM and Nicolescu S (2005) World skarn deposits. In *Economic Geology, 100th Anniversary Volume* (eds JW Hedenquist, JFH Thompson, RJ Goldfarb and JP Richards), pp. 299–336. Littleton, Colorado: Society of Economic Geologists.

Middlemost EAK (1972) A simple classification of volcanic rocks. *Bulletin of Volcanology* **36**, 382–97.

Middlemost EAK (1994) Naming materials in the magma/igneous rock system. *Earth Science Reviews* **37**, 215–24.

Mustard R, Ulrich T, Kamenetsky VS and Mernagh T (2006) Gold and metal enrichment in natural granitic melts during fractional crystallization. *Geology* **34**, 85–8.

Newberry RJ and Swanson SE (1986) Scheelite skarn granitoids: an evaluation of the roles of magmatic source and process. *Ore Geology Review* **1**, 57–81.

Ouyang HG and Che XG (2016) ^{40}Ar-^{39}Ar dating of Ergu Fe-polymetalic skarn deposit in Yichun igneous belt and its geological implications. *Mineral Deposits* **35**, 1035–46 (in Chinese with English abstract).

Patiño Douce AE and Harris N (1998) Experimental constraints on Himalayan anatexis. *Journal of Petrology* **39**, 689–710.

Pearce JA, Harris NBW and Tindle AG (1984) Trace element discrimination diagrams for the tectonic interpretation of granitic rocks. *Journal of Petrology* **25**, 956–83.

Pearce JA and Norry MJ (1983) Role of the subcontinental lithosphere in magma genesis at active continental margins. In *Continental Basalts and Mantle Xenoliths* (ed. CJ Hawkesworth), pp. 230–49. Nantwich, Cheshire: Shiva Publications.

Peccerillo A and Taylor SR (1976) Geochemistry of eocene calc-alkaline volcanic rocks from the Kastamonu area, Northern Turkey. *Contributions to Mineralogy and Petrology* **58**, 63–81.

Pitcher WS (1997) *The Nature and Origin of Granite* (2nd edition). London: Chapman & Hall, 386 pp.

Pons J, Franchini M, Meinert L, López-Escobar L and Maydagán L (2010) Geology, petrography and geochemistry of igneous rocks related to mineralized skarns in the NW Neuquén basin, Argentina: implications for Cordilleran skarn exploration. *Ore Geology Review* **38**, 37–58.

Pu W, Gao JF, Zhao KD, Ling HF and Jiang SY (2005) Separation method of Rb-Sr, Sm-Nd using DCTA and HIBA. *Journal of Nanjing University (Natural Sciences)* **41**, 445–50 (in Chinese with English abstract).

Qiu JT, Yu XQ, Santosh M, Zhang DH, Chen SQ and Li JP (2013) Geochronology and magmatic oxygen fugacity of the Tongcun molybdenum deposit, northwest Zhejiang, SE China. *Mineralogica Deposita* **48**, 545–56.

Ren JS, Niu BG and Liu ZG (1999) Soft collision, superposition orogeny and polycyclic suturing. *Earth Science Frontiers* **6**, 85–93 (in Chinese with English abstract).

Ren L (2017) *Study on the diagenesis mechanisms and metallogenic model of skarn-type Fe-Cu (Mo) polymetallic deposit in the Lesser Xing'an Range, NE China*. Master degree thesis), Jilin University, Changchun (in Chinese with English abstract).

Ren L, Sun JG, Han JL, Liu Y, Wang CS, Gu AL, Zhao KQ and Yu RD (2017) Magmatism and metallogenic mechanisms of the Baoshan Cu-polymetallic deposit from the Lesser Xing'an Range, NE China: constraints from geology, geochronology, geochemistry, and Hf isotopes. *Ore Geology Review* **88**, 270–88.

Richards JP (2003) Tectono-magmatic precursors for porphyry Cu-(Mo-Au) deposit formation. *Economic Geology* **98**, 1515–33.

Richards JP (2011) High Sr/Y arc magmas and porphyry Cu ± Mo ± Au deposits: just add water. *Economic Geology* **106**, 1075–81.

Ridolfi F, Renzulli A and Puerini M (2010) Stability and chemical equilibrium of amphibole in calc-alkaline magmas: an overview, new thermobarometric formulations and application to subduction-related volcanoes. *Contributions to Mineralogy and Petrology* **160**, 45–66.

Robb L (2005) *Introduction to Ore-Forming Processes*. Malden: Blackwell Publishing, —373 pp.

Rudnick RL, Gao S, Ling WL, Liu YS and McDonough WF (2004) Petrology and geochemistry of spinel peridotite xenoliths from Hannuoba and Qixia, North China Craton. *Lithos* **77**, 609–37.

Saunders AD, Norry MJ and Tarney J (1988) Origin of MORB and chemically-depleted mantle reservoirs: trace element constraints. *Journal of Petrology* **1**, 415–45.

Shi PH, Yang YC, Ye SQ and Han SJ (2012) Geological and geochemical characteristics and genesis of ferromolybdenum deposit in Wudaoling, Heilongjiang Province. *Global Geology* **31**, 262–70 (in Chinese with English abstract).

Shu Q-H, Chang Z-S, Lai Y, Zhou Y-T, Sun Y and Yan C (2016) Regional metallogeny of Mo-bearing deposits in northeastern China, with new Re-Os dates of porphyry Mo deposits in the northern Xilamulun district. *Economic Geology* **111**, 1783–98.

Sillitoe RH (2010) Porphyry copper systems. *Economic Geology* **150**, 3–41.

Sisson TW (1994) Hornblende-melt trace-element partitioning measured by ion microprobe. *Chemical Geology* **117**, 331–44.

Soesoo A (2000) Fractional crystallization of mantle-derived melts as a mechanism for some I-type granite petrogenesis: an example from Lachlan Fold Belt, Australia. *Journal of the Geological Society* **157**, 135–49.

Sun DY, Wu FY and Gao S (2004) LA-ICP-MS zircon U-Pb age of the Qingshui pluton in the East Xiao Hinggan Mountains. *Acta Geoscientifica Sinica* **25**, 213–18 (in Chinese with English abstract).

Sun JG, Zhang Y, Han SJ, Men LJ, Li YX, Chai P and Yang F (2013) Timing of formation and geological setting of low-sulphidation epithermal gold deposits in the continental margin of NE China. *International Geological Review* **55**, 608–32.

Sun JG, Zhang Y, Xing SW, Zhao KQ, Zhang ZJ, Bai LA, Ma YB and Liu YS (2012) Genetic types, ore-forming age and geodynamic setting of endogenic molybdenum deposits in the eastern edge of Xing-Meng orogenic belt. *Acta Geoscientifica Sinica* **28**, 1317–32 (in Chinese with English abstract).

Sun SS and McDonough WF (1989) Chemical and isotopic systematics of oceanic basalts: implications for mantle composition and processes. In *Magmatism in the Ocean Basins* (ed. AD Saunders), pp. 313–45. Geological Society of London, Special Publication no. 42.

Sun WD, Arculus RJ, Kamenetsky VS and Binns RA (2004) Release of gold-bearing fluids in convergent margin magmas prompted by magnetite crystallization. *Nature* **431**, 975–8.

Sun WD, Huang R, Li H, Hu Y, Zhang C, Sun S, Zhang L, Ding X, Li C, Zartman RE and Ling M (2015) Porphyry deposits and oxidized magmas. *Ore Geology Review* **65**, 97–131.

Sylvester PJ (1998) Post-collisional strongly peraluminous granites. *Lithos* **45**, 29–44.

Tan HY (2013) *Metallogenetic series and prospecting assessment in Lesser Xing'an Range-Zhangguangcai Range metallogenic belt of Heilongjiang Province*. M.S thesis, China University of Geosciences, Beijing, China (in Chinese with English abstract).

Tomurtogoo O, Windley BF, Kroner A, Badarch G and Liu DY (2005) Zircon age and occurrence of the Adaatsag ophiolite and Muron shear zone, central Mongolia: constraints on the evolution of the Mongol-Okhotsk ocean, suture and orogen. *Journal of the Geological Society, London* **162**, 125–34.

Trail D, Watson EB, Tailby ND (2012) Ce and Eu anomalies in zircon as proxies for oxidation state of magmas. *Geochimica et Cosmochimica Acta* **97**, 70–87.

Van der Voo R, Spakman W and Bijwaard H (1999) Mesozoic subducted slabs under Siberia. *Nature* **397**, 246–9.

Vervoort JD and Blichert-Toft J (1999) Evolution of the depleted mantle: Hf isotope evidence from juvenile rocks through time. *Geochimica et Cosmochimica Acta* **63**, 533–56.

Wang F, Xu WL, Gao FH, Zhang HH, Pei FP, Zhao L and Yang Y (2014) Precambrian terrane within the Songnen-Zhangguangcai Range Massif, NE China; evidence from U-Pb ages of detrital zircons from the Dongfengshan and Tadong groups. *Gondwana Research* **26**, 402–13.

Wang L, Yang YC, Zhang GB and Li HY (2013) Chronology, geochemical characteristics and genesis of Qiupigou copper deposit in Heilongjiang. *Global Geology* **32**, 24–34 (in Chinese with English abstract).

https://doi.org/10.1017/S0016756821000479 Published online by Cambridge University Press

Wang ZW, Xu WL, Pei FP, Wang F and Guo P (2016) Geochronology and geochemistry of early Paleozoic igneous rocks of the Lesser Xing'an Range, NE China: implications for the tectonic evolution of the eastern Central Asian Orogenic Belt. *Lithos* **261**, 144–63.

Wei HY (2012) *The geochronology and petrogenesis of granite in Yichun-Hegang area, Heilongjiang Province*. Master degree thesis, Jilin University, Changchun, China (in Chinese with English abstract).

Whalen JB, Currie KL and Chappell BW (1987) A-type granites: geochemical characteristics, discrimination and petrogenesis. *Contributions to Mineralogy and Petrology* **95**, 407–19.

Windley BF, Alexeiev D, Xiao WJ, Kröner A and Badarch G (2007) Tectonic models for accretion of the Central Asian Orogenic Belt. *Journal of the Geological Society, London* **164**, 31–47.

Wu FY, Jahn BM, Wilde S and Sun DY (2000) Phanerozoic crustal growth. U-Pb and Sr-Nd isotopic evidence from the granites in northeastern China. *Tectonophysics* **328**, 89–113.

Wu FY, Jahn BM, Wilde SA, Lo CH, Yui TF, Lin Q, Ge WC and Sun DY (2003) Highly fractionated I-type granites in NE China (II): isotopic geochemistry and implications for crustal growth in the Phanerozoic. *Lithos* **67**, 191–204.

Wu FY, Sun DY, Ge WC, Zhang YB, Grant ML, Wilde SA and Jahn BM (2011) Geochronology of the Phanerozoic granitoids in northeastern China. *Journal of Asian Earth Sciences* **41**, 1–30.

Wu FY, Yang JH, Lo CH, Wilde SA, Sun DY and Jahn BM (2007) The Heilongjiang Group: a Jurassic accretionary complex in the Jiamusi Massif at the western Pacific margin of northeastern China. *Journal of Asian Earth Sciences* **30**, 542–56.

Xiao WJ, Windley BF, Hao J and Zhai MG (2003) Accretion leading to collision and the Permian Solonker suture, Inner Mongolia, China: termination of the central Asian orogenic belt. *Tectonics* **22**, 1069–89.

Xie GQ, Mao JW, Zhu QQ, Yao L, Li YH, Li W and Zhao HJ (2015) Geochemical constraints on Cu-Fe and Fe skarn deposits in the Edong district, Middle-Lower Yangtze River metallogenic belt, China. *Ore Geology Review* **64**, 425–44.

Xu MJ, Xu WL, Wang F, Gao FH and Yu JJ (2013) Geochronology and geochemistry of the Early Jurassic granitoids in the central Lesser Xing'an Range, NE China and its tectonic implications. *Acta Petrologica Sinica* **29**, 354–68 (in Chinese with English abstract).

Xu ZT, Sun JG, Liang XL, Xu ZK and Chu XL (2020) Geochronology, geochemistry, and Pb-Hf isotopic composition of mineralization-related magmatic rocks in the Erdaohezi Pb-Zn Polymetallic Deposit, Great Xing'an Range, Northeast China. *Minerals* **10**(3). doi: 10.3390/min10030274.

Yang F (2013) *The study on mineralization and metallogenic background of Dan'anhe gold deposit in Yichun, Heilongjiang Province*. Master degree thesis, Jilin University, Changchun, China (in Chinese with English abstract).

Yang JH, Wu FY, Shao JA, Wilde SA, Xie LW and Liu XM (2006) Constraints on the timing of uplift of the Yanshan fold and thrust belt, North China. *Earth and Planetary Science Letters* **246**, 336–52.

Yang YC, Han SJ, Sun DY, Guo J and Zhang SJ (2012) Geological and geochemical features and geochronology of porphyry molybdenum deposits in the Lesser Xing'an Range-Zhangguangcai Range metallogenic belt. *Acta Petrologica Sinica* **28**, 379–90 (in Chinese with English abstract).

Yao L, Lü ZC, Zhao CS, Pang ZS, Yu XF, Yang T, Li YS, Liu P and Zhao MC (2017) Zircon U-Pb geochronological, trace element, and Hf isotopic constraints on the genesis of the Fe and Cu skarn deposits in the Qiman Tagh area, Qinghai Province, Eastern Kunlun Orogen, China. *Ore Geology Review* **91**, 387–403.

Yu JJ, Wang F, Xu WL, Gao FH and Pei FP (2012) Early Jurassic mafic magmatism in the Lesser Xing'an– Zhangguangcai Range, NE China, and its tectonic implications: constraints from zircon U-Pb chronology and geochemistry. *Lithos* **142–143**, 256–66.

Zartman RE and Doe BR (1981) Plumbotectonics – the model. *Tectonophysics* **75**, 135–62.

Zhang DH, Zhou SH, Wan TF, Xi BB and Li JP (2007) Depth of ore deposit formation and prognosis of deep-seated ore deposits. *Geological Bulletin of China* **26**, 1509–18.

Zhang Y (2013) *Research on characteristics of geology, geochemistry and metallogenic mechanism of the Jurassic molybdenite deposits in the Mid- East area of Jilin*. MS thesis, Jilin University, Changchun, China (in Chinese with English abstract).

Zhang Y, Sun JG, Xing SW and Zhang ZJ (2018) Geochronology and geochemistry of the Cuihongshan Fe-polymetallic deposit, northeastern China: implications for ore genesis and tectonic setting. *Canadian Journal of Earth Sciences* **55**, 475–89.

Zhang ZC, Mao JW, Wang YB, Pirajno P, Liu JL and Zhao ZD (2010) Geochemistry and geochronology of the volcanic rocks associated with the Dong'an adularia–sericite epithermal gold deposit, Lesser Hinggan Range, Heilongjiang province, NE China: constraints on the metallogenesis. *Ore Geology Review* **37**, 158–74.

Zhao HL (2014) *Ore genesis and geodynamic settings of tungsten deposits in eastern Jilin and Heilongjiang Provinces*. MS thesis, Jilin University, Changchun, China (in Chinese with English abstract).

Zhao K, Xu XS, and Erdmann S (2017) Crystallization conditions of peraluminous charnockites: constraints from mineral thermometry and thermodynamic modelling. *Contributions to Mineralogy and Petrology* **172**(5), 26.

Zhao YM, Feng CY, Li DX, Liu JN, Xiao Y, Yu M and Ma SC (2013) Metallogenic setting and mineralization-alteration characteristics of major skarn Fe-polymetallic deposits in Qimantag area, western Qinhai Province. *Mineral Deposits* **32**, 1–19 (in Chinese with English abstract).

Zhao ZH, Sun JG, Li GH, Xu WX, Lv CL, Wu S, Guo Y, Liu J and Ren L (2019) Early Cretaceous gold mineralization in the Lesser Xing'an Range of NE China: the Yongxin example. *International Geology Review* **61**, 1522–48.

Zhong SH, Feng CY, Reimar S, Li DX and Dai ZH (2018) Geochemical contrasts between Late Triassic ore-bearing and barren intrusions in the Weibao Cu-Pb-Zn deposit, East Kunlun Mountains, NW China: constraints from accessory minerals (zircon and apatite). *Mineralogica Deposita* **53**, 855–70.

Zhou J-B, Wilde SA, Zhang X-Z, Zhao G-C, Zheng C-Q, Wang Y-J and Zhang X-H (2009) The onset of Pacific margin accretion in NE China: evidence from the Heilongjiang high-pressure metamorphic belt. *Tectonophysics* **478**, 230–46.

Zou XY, Qin KZ, Han XL, Li GM, Evans NJ, Li ZZ and Yang W (2019) Insight into zircon REE oxy-barometers: a lattice strain model perspective. *Earth and Planetary Science Letters* **506**, 87–96.